What is the Role of Non-Fullerene Acceptor Symmetry in Polymer Solar Cell Efficiency?

Guoping Li [1, #], Fei Qin [1, 2, #], Robert M. Jacobberger [1], Subhrangsu Mukherjee [2], Leighton O. Jones [1], Ryan M. Young [1,], Robert M. Pankow [1], Brendan P. Kerwin [1], Lucas Q. Flagg [3], Ding Zheng [1], Liang-wen Feng [6], Kevin L. Kohlstedt [1,*], Vinod K. Sangwan [3,*], Mark C. Hersam [1,4,*], George C. Schatz [1,*], Dean M. DeLongchamp [3,*], Michael R. Wasielewski [1,*] Yinhua, Zhou [2,*], Antonio Facchetti [1,5,*], and Tobin J. Marks [1,3*]

[1] Department of Chemistry, Center for Light Energy Activated Redox Processes (LEAP), and the Materials Research Center (MRC), Northwestern University, 2145 Sheridan Road, Evanston, Illinois 60208, United States

[2] Wuhan National Laboratory for Optoelectronics, Huazhong University of Science and Technology, Wuhan 430074, China.

[3] Material Measurement Laboratory, National Institute of Standards and Technology, Gaithersburg, Maryland 20899, United States

[4] Department of Materials Science and Engineering, and the Materials Research Center (MRC),Northwestern University, Evanston, Illinois 60208, United States

[5] Flexterra Corporation, 8025 Lamon Avenue, Skokie, Illinois 60077, United States

[6] Key Laboratory of Green Chemistry &Technology, Ministry of Education, College of Chemistry, Sichuan University, Chengdu 610065, China

Keywords

Polymer solar cells, non-fullerene acceptor, conformation effect, noncovalently intramolecular interactions, power conversion efficiency

Context & Scale

The rapid development of bulk-heterojunction (BHJ) polymer solar cells (PSCs) composed of non-toxic, mechanically durable organic materials has dramatically elevated light-to electricity power conversion efficiencies (PCEs) beyond 19%. However, these advances have largely relied on non-fullerene acceptors (NFAs) having symmetric A-D-A or A-DAD-A architectures. Intense exploratory efforts have focused on NFA elaboration, probing diverse architectures and substitutions. Nevertheless, symmetric architectures have prevailed in PCE and the reasons underlying this apparent universality are not well understood. Here we synthesize/characterize/compare/contrast in detail, using crystallographic, morphological, photovoltaic, opto-electronic, and DFT analyses, the behaviors of two sets of NFAs differing principally in their architectural symmetry. The results indicate that NFA symmetry not only impacts acceptor molecular photophysical properties, but also affects crystallinity, charge carrier dynamics, and photo-generated exciton transport. We also conclude that while asymmetric acceptors can efficiently split excitons, the separated excitons have shorter lifetimes/more rapid recombination, reflecting the absence of continuous intermolecular EG···EG π-π stacking. These results shed light on the role of NFA symmetry in PSC performance and convey design implications for future higher-performance PSCs.

Summary

Molecular-level design of non-fullerene acceptors (NFAs) plays an essential role in bulk-heterojunction (BHJ) polymer solar cells (PSCs) and has elevated power conversion efficiencies (PCEs) beyond 19%. While most successful NFAs have *symmetric* Acceptor-Donor-Acceptor (A-D-A) or A-DA'D-A architectures, there is minimal understanding of how NFA symmetry influences BHJ PSC performance. Here we report a new NFA series with closely related *asymmetric* D-D-A and D-DA'D-A architectures and compare/contrast their properties with traditional symmetric NFAs. We find that BHJ PSC performance with PM6 and PBDB-T donor polymers and symmetric NFAs (PCE =10-17 %) greatly exceeds that with the corresponding asymmetric NFAs (PCE = 0.1 - 3 %). The reason is far lower current densities and fill factors of the latter cells, while the open circuit voltages remain comparable. Single-crystal diffraction indicates that the asymmetric NFAs do not engage in continuous endgroup···endgroup π-π stacking, essential for efficient electron mobility, and consistent with electron-only mobility data. While DFT analysis reveals lower internal reorganization energies and stronger π-π-coupling within asymmetric NFA dimers, AFM morphology and 2D-GIWAXS indicate that the asymmetric NFAs are overall less crystalline, not forming textured domains in the BHJ blends. Time-resolved transient absorption, electron paramagnetic resonance, and impedance analysis reveal slower hole transfer in BHJs with asymmetric acceptors and strongly bound charge transfer states, supporting energy decay via triplet states, higher rates of exciton recombination, and lower yields of free charge carriers. This information should inform the design of future high-performance NFAs.

Introduction

Bulk-heterojunction (BHJ)-based polymer solar cells (PSCs) with efficient solar energy harvesting are promising for future renewable energy production.[1-3] Compared with traditional inorganic photovoltaics, PSCs can be mechanically flexible, light-weight, based on non-toxic earth-abundant elements, and enable inexpensive solar module production by printing, which makes them ideal alternatives to current technologies.[4-16] However, due to the intrinsic properties of organic semiconducting materials, a non-trivial energy (voltage) loss occurs during the exciton to charge generation process(typically ~1.0 eV in fullerene-based PSCs, ~0.6 eV in non-fullerene based PSCs, and ~ 0.3 eV in perovskite solar cells),[17-20] limiting the power conversion efficiencies (PCEs) of state-of-art PSCs versus the leading inorganic counterparts. [21,22]

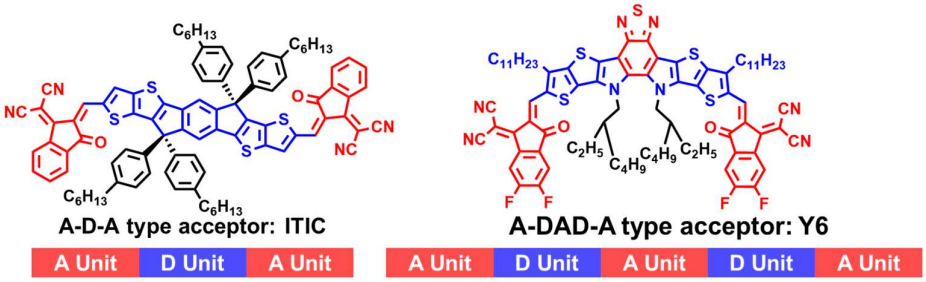

Figure 1. NFA symmetrical D−A architectures. Left: Representative A-D-A type NFA architecture**: ITIC**; Left: Representative A-DAD-A type NFA: **Y6.**

Since the first development of **ITIC**-based non-fullerene acceptors (NFAs) by Zhan et al, [23-25]. tremendous efforts have been dedicated to enhance NFA PSCs by tuning the molecular structures and properties, which in most cases yielded energy losses comparable to fullerene-based acceptors.[24,26-28] Notably, the second-generation NFAs, such as **Y6** (**Figure 1**), by Yuan et al, [29-31] further increased PSC current densities while retaining low energy losses. Some other recently reported NFAs using the **Y6**-skeleton have achieved over 18% PCE in binary cells, [32-36] over 19% in ternary cells (small-area devices) and over 10% large-area modules.[37-41] Viewing these high-performance NFAs together, it is clear that nearly all are based on a symmetric *'A-D-A or A-DAD-A'* architectures, where A and A' represent the electron-accepting fragments, and D the electron-donating fragments.[42-44] Some high-performance asymmetric NFAs reported recently employ different A end groups (EGs), but essentially still have the same symmetric

'A-D-A or A- DA'D-A architecture (**Figure 1**).[45-50] Also, it is challenging to synthesize these acceptors with different EGs on each side of the molecule in large scale due to the low yields of asymmetric fused-ring condensation reactions and the difficulties occurring during the laborious purification process. Furthermore, it can be seen that nearly all of the high-performance NFAs reported to date are built around the indaceno[1,2-b:5,6-b']dithiophene (**IDT**) electron-donating core end-capped with IC (2-(3-oxo-2,3-dihydroinden-1-ylidene)malononitrile) electron-accepting end groups (EGs) on either core side.[51-53] However, a fundamental question remains as why this symmetric NFA architecture is so unique and photovoltaically effective. Some studies have suggested that the intramolecular D-A coupling that enables the intermolecular charge transfer (ICT) is essential for efficient exciton generation.[54-57] It has also been shown that when NFAs are blended with donor polymers and processed into thin films they generally retain the packing motifs found in their single-crystal structures, which promotes efficient electron transport networks in the acceptor domains.[58-60] The IC-based π-π stacking serves as an essential structural feature for the charge transporting networks promoting photocurrent density.[31,61] Compared with acceptor materials lacking IC EGs (small molecules and polymer acceptors), such as rhodamine-types[62,63], DPP-types polymer acceptors[64-66] and NDI-type acceptors[67,68], the acceptors with IC EGs exhibit more efficient and balanced charge carrier transport. However, it remains unknown why efficient electron transport networks and large photon-to charge conversion requires the D-A couplings to be arranged symmetrically around the molecular core. This is the scientific question we seek to answer in this study.

In this work, two sets of symmetric NFAs with the traditional IDT-core (*A-D-A architecture*) and the recently developed high-performance Y6-core (*A-DA'D-A architecture*), having π-extended IC EGs, [31,69] along with the corresponding asymmetric derivatives (*D-D-A and D-DA'D-A architectures*) where one IC EG is replaced with electron-donating thiophene (T) and thieno[3,2-b]thiphene (TT) units are synthesized and characterized (**Figure 2**). There are two reasons we choose T and TT as electron-donating units to constructure the asymmetric acceptors: 1) synthetic accessibility, and 2) similartity to the current state-of-art high-performance NFAs. The focus of this study is to explore the

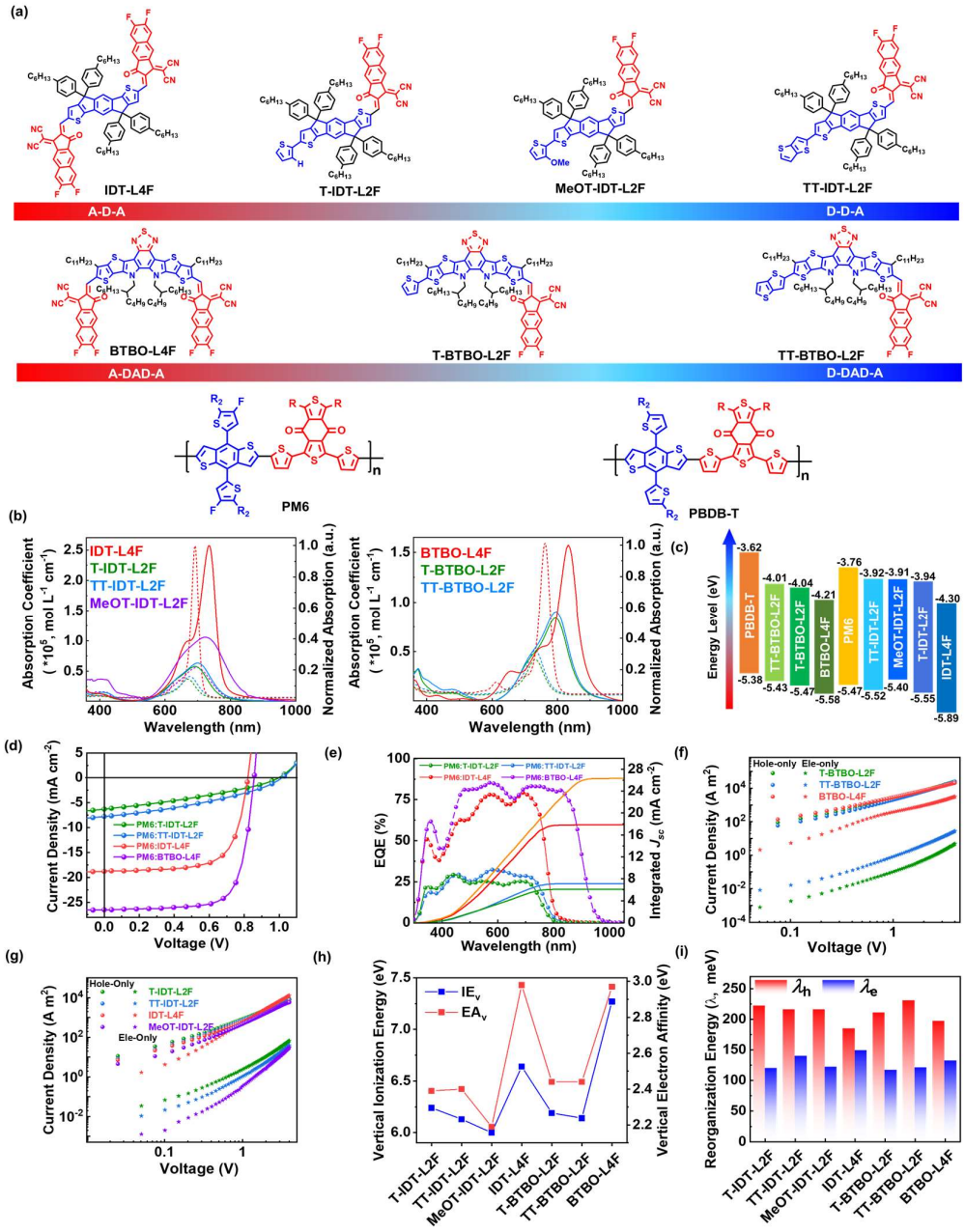

Figure 2. (a). Molecular structures of acceptors **T-IDT-L2F, TT-IDT-L2F, MeOT-IDT-L2F, IDT-L4F, T-BTBO-L2F, TT-BTBO-L2F, BTBO-L4F**, and donor polymers **PBDB-T** and **PM6** (R= 2-ethylhexyl) **(b)**. Absorption coefficients in chloroform solution (dotted line) and thickness-normalized film absorption spectra (solid line) of acceptors. **(c)**. Frontier orbital energetics of all acceptors and donor polymers in this study. The HOMO is estimated from cyclic voltammetry, and the LUMO is calculated from the optical bandgap E_g^{opt}, where $E_g^{opt} = 1240/\lambda_{onset,\ film}$. **(d)** PSC current–voltage (J–V) characteristics; **(e)** Corresponding external quantum efficiencies (EQEs) data for the indicated blends; and **(f)** IDT-core based and **(g)** BTBO-core based blend hole-only and electron-only mobilities measured by SCLC with PM6 as the donor. **(h)** Vertical ionization energy (IEv) and vertical electron affinity (EAv) of the NFAs. **(i)** Computed internal reorganization energies (IREs, λe) of the isomers of the indicated NFAs. The data of BTBO-L4F was taken from our previous work (ref.14). Copyright: American Chemical Society, 2022.

to be as close to the current state-of-art NFA as possible, such that we can compare the difference in device performance with symmetric acceptors and asymmetric acceptors in a straightforward way. BHJ PSCs are fabricated, and the photovoltaic data indicate that the symmetric NFAs far outperform the asymmetric counterparts. With a combination of single-crystal analysis, space-charge-limited current (SCLC) data, density functional theory (DFT) analysis, two-dimensional-grazing incidence wide-angle X-ray scattering (2D-GIWAXS), atomic force microscopy (AFM), femto/nanosecond transient absorption (fs/ns TA), electron paramagnetic resonance (EPR) spectroscopy, and impedance-based integrated photocurrent device analysis (IPDA), we find that NFA architectural symmetry not only influences the charge carrier dynamics, but also plays an essential role in determining the acceptor physical properties, the behavior of the photo-generated excitons, and the BHJ layer morphology (*vide infra*).

Results and Discussion

Molecular structures and photophysical properties

The chemical structures of the NFAs used in this study, **T-IDT-L2F**, **TT-IDT-L2F**, **MeOT-IDT-L2F**, **IDT-L4F**, **T-BTBO-L2F**, **TT-BTBO-L2F**, **BTBO-L4F**, and polymer donors **PBDB-T** and **PM6** are shown in **Figure 2a**. Synthetic and experimental details are reported in the Supporting Information (**SI**, **Section S2**). To fully examine the role of symmetry, two symmetric NFAs, **IDT-L4F**, and **BTBO-L4F**,[31] end-capped with two π-extended and fluorinated EG groups (**L4F**), were synthesized for comparison. By removing an EG group from **IDT/BTBO-L4F** and replacing it with one thiophene (T) or thieno[3,2-b]thiophene (TT) unit, the four new asymmetric acceptors were obtained using a Stille coupling protocol (see SI for details). Substitution of an electron-accepting **L4F** unit with an electron-donating T or TT unit strongly affects the overall dipole moments of these molecules and the number of π-electrons in the π-conjugated system. Therefore, the optical absorption profiles are significantly impacted. From the optical absorption data in solution (**Figure 2b** and **Table 1**), it is clear that the solution absorption coefficient of the asymmetric acceptors (10^4 mol L^{-1} cm^{-1}) is about one order of magnitude lower than their symmetric counterparts (10^5 mol

L^{-1} cm^{-1}). Similarly, the normalized film absorption spectrum of the symmetric NFAs, is greater but within a factor of ~ 2x versus the asymmetric NFAs, which should not be the main root for the disparity in device performance (*vide infra*), since: (1) the light absorption region of the asymmetric acceptors still encompasses most of the visible light region and is only slightly blue-shifted by 10-30 nm versus their symmetric counterparts; (2) the solution absorption coefficients of the asymmetric acceptors are still 5-10 fold greater those of the traditional fullerene acceptors, e.g., $PC_{61}BM$[70], which can deliver PCEs > 7%.[71,72] When spin-coated into films, all acceptors exhibit red-shifted absorption spectra versus those in solution, indicating that all of these acceptors are able to form π-π stacked aggregates. However, for both NFA sets, the asymmetric acceptors have reduced red-shifted absorption *vs* their symmetric counterparts (**Table 1**) with the IDT-core-NFAs being smaller than the BTBO-core-based analogues. Therefore, we suggest that the reduced red-shift of the asymmetric acceptor molecules can be ascribed to the fewer π-electrons rather than the asymmetric architectures.

The frontier molecular orbital (FMO) energies of all acceptors were assessed by both cyclic voltammetry (CV) and ultraviolet photoelectron spectroscopy (UPS). The highest occupied molecular orbital (HOMO) energies estimated from the two techniques are in good agreement with each other (**SI Figure S25, Table S2**). The lowest unoccupied molecular orbital (LUMO) energies were then calculated based on the optical bandgaps. The results are plotted in **Figure 2c.** Note that even with more π-electrons included in the conjugation, the symmetric acceptors still have lower-lying HOMOs (**IDT-L4F**: -5.89 eV,

Table 1. Summary of acceptor optical properties.

Acceptor	λ_{max}, nm		λ_{onset}, nm			
	Solution[c]	Film[b]	Solution[c]	Film[b]	$\Delta\lambda_{max}$, nm	E_g [opt a]
T-IDT-L2F	668	692	730	765	24	1.62
MeOT-IDT-L2F	698	725	782	830	27	1.49
TT-IDT-L2F	675	700	728	775	25	1.60
IDT-L4F	691	735	720	780	44	1.59
T-BTBO-L2F	733	793	780	868	60	1.43
TT-BTBO-L2F	735	797	782	873	62	1.42
BTBO-L4F	762	837	822	934	75	1.32

[a]Optical band gap was calculated by $1240/\lambda_{onset}$, film. [b]Film absorption was recorded from spin-coated film from 5.0 mg/mL solutions. [c]Solution absorption was recorded in 0.0050 mg/mL chloroform solution.

BTBO-L4F: -5.58 eV) and LUMO (**IDT-L4F**: -4.30 eV, **BTBO-L4F**: -3.92 eV) than their asymmetric counterparts (**T-IDT-L2F**: HOMO -5.55 eV, LUMO -3.94eV, **T-BTBO-L2F**: HOMO -5.47 eV, LUMO -4.04 eV), suggesting that the electron-withdrawing L2F EGs dominate the energetics of the acceptors. Based on the energy level of these acceptors, the popular donor polymers **PBDB-T** and **PM6**, which both possess suitable energy levels to form type-II BHJs, were selected to pair with these NFAs for device fabrication and opto-electronic properties characterization.

Photovoltaic response and carrier mobility

To probe NFA symmetry effects on the photovoltaic properties, conventional PSCs with structure, ITO-glass/hole transport layer/ BHJ active layer/electron transport layer/Ag, were fabricated. To minimize the fabrication-related performance variations among devices, the identical parameters (spin rate, D:A mass ratio and annealing conditions) were utilized across all the blends with the same molecular core (see details in **SI section S8**). The results are summarized in **Table 2** and **Figures 2d-e**. Note that the symmetric acceptors, **IDT-L4F** and **BTBO-L4F**, exhibit respectable PCEs of 10.55% and 16.30% when blended with PM6, respectively. The high current density (J_{SC}) of 27.61 mA cm^{-2} and fill factor (FF) of 70.2% suggest efficient exciton generation-charge-separation-charge collection processes within the BHJ active layer of these symmetric acceptors.

Note that the 10.55% PCE obtained for **IDT-L4F** is one of the highest recorded to date for IDT-core-based acceptors. However, the PCEs of the **PM6**:asymmetric acceptor PSCs are far lower--only ~ 2% for IDT NFAs and negligible for BTBO-core-based NFAs. The lower performance of the asymmetric NFAs mainly reflects the low J_{SC} (1.3 – 7.8 mA/cm^2) and FF (30-40%) values. Since the energetics of **PM6:T-BTBO-L2F** and **TT-BTBO-L2F** blends are not type-II heterojunctions, we fabricated devices using the polymer donor, **PBDB-T**, which possesses higher-lying HOMOs and LUMOs (**Figure 2c**). However, the PCEs of these PSCs remain low (1.3 -3.8 %; **Table 2**), again reflecting the depressed J_{sc}s and FFs.

The open-circuit voltages (V_{oc}) generated by all the present cells are in the expected range for the orbital energetics involved, and are found to be 0.83-0.84 V for the symmetric

NFA based devices and 0.93-1.01 V for the asymmetric NFA based devices (**Table 2**). If the voltage loss is estimated by the Shockley–Queisser (SQ) equation,[73] $\triangle V_{oc,}{}^{loss} = E^{opt}{}_g - q^*V_{OC}$, where $E^{opt}{}_g$ is the optical bandgap, and q* is the unit charge, it can be seen that the voltage loss of the asymmetric acceptors is slightly lower than that of the symmetric counterparts even though the latter have much higher PCEs. This result suggests that the asymmetric architecture does not directly impact the voltage loss of these devices, and excitons generated upon irradiation can be efficiently split in all blends. This is consistent with the findings from time-resolved transient absorption, where fast hole transfer occurs in both the asymmetric and symmetric acceptor blends (*vide infra*). Therefore, there are two possible reasons for the much lower PSC performance produced by the NFAs with asymmetric architectures: 1) The lower fill factor argues that the asymmetric acceptors form far less textured domains in the blend, resulting in a suboptimal blend film morphology, which hampers the exciton transport. 2) The lower current density implies that while excitons can form and split in the asymmetric NFA based blends, the charge carriers are not efficiently transported (or trapped) by the asymmetric acceptor crystalline domains due to the poor stacking motifs (see more below).

Table 2. Summary of the photovoltaic performance parameters and charge carrier mobilities for the indicated PSC blends.

Donor	Acceptor	V_{OC} (V)	J_{SC} (mA/cm^2)	FF (%)	PCE[b] (%)
PM6	IDT-L4F	0.83 (0.83±0.01)	18.08 (17.71±0.33)	70.1 (70.5±0.4)	10.52 (10.36±0.14)
	T-IDT-L2F	1.00 (0.99±0.01)	6.29 (6.09±0.12)	33.1 (32.5±0.3)	2.08 (1.97±0.07)
	TT-IDT-L2F	1.01 (1.01±0.01)	7.76 (7.07±0.57)	36.0 (35.5±0.5)	2.84 (2.59±0.19)
	TT-IDT-L2F[a]	0.93 (0.92±0.01)	0.15 (0.14±0.01)	29.5 (29.2±0.4)	0.04 (0.03±0.01)
	MeOT-IDT-L2F	0.96(0.95±0.02)	1.32 (1.25±0.09)	33.2 (34.3±2.2)	0.42 (0.40±0.01)
	BTBO-L4F	0.84(0.84±0.01)	27.61(27.08±0.53)	70.2 (69.7±0.4)	16.30 (16.05±0.25)
	T-BTBO-L2F	0.92(0.92±0.01)	< 10^{-1}	\	\
	TT-BTBO-L2F	0.91(0.91±0.01)	< 10^{-1}	\	\
PBDB-T	IDT-L4F	0.61 (0.60±0.01)	13.66 (11.69±1.43)	43.0 (42.1±0.6)	3.57 (2.97±0.40)
	T-IDT-L2F	0.86 (0.84±0.01)	9.04 (8.76±0.15)	35.0 (35.3±0.3)	2.71 (2.62±0.06)
	MeOT-IDT-L2F	0.87 (0.87±0.01)	6.16 (5.98±0.18)	25.2 (34.8±0.9)	1.35 (1.26±0.09)
	TT-IDT-L2F	0.88 (0.87±0.01)	11.3 (10.11±0.85)	38.9 (38.1±0.9)	3.87 (3.37±0.29)
	BTBO-L4F	0.68 (0.67±0.02)	25.06 (24.38±0.58)	63.4 (61.1±2.73)	10.73 (10.04±0.67)
	T-BTBO-L2F	0.87 (0.85±0.01)	5.92 (5.65±0.21)	43.4 (42.9±0.7)	2.22 (2.07±0.11)
	TT-BTBO-L2F	0.84 (0.85±0.02)	5.71 (5.41±0.16)	42.2 (42.2±0.6)	2.03 (1.93±0.08)

[a] Fabricated with D: A mass ratio = 1: 4. [b] Photovoltaic and charge mobility data reported as averages taken over 10 separate devices where the ± represents one standard deviation from the mean.

Besides attempting morphological manipulations, we also attempted to increase the asymmetric acceptor weight content in the BHJ precursor blend during device fabrication, hoping this would increase the acceptor density and promote formation of more acceptor domains. However, even when the donor: acceptor mass ratio is increased to 1:4 (**Table 2**), the current density in the asymmetric acceptor blend remains low. Another approach from the chemistry standpoint would be to increase the crystallinity of the asymmetric acceptor, so as to form more crystalline domains in the BHJ film. Thus, we replaced the **T-IDT-L2F** with **TT-IDT-L2F** and **MeOT-IDT-L2F**. The S···O conformational locks can promote the planarity of the **MeOT-IDT-L2F** by locking the rotation of the thiophene ring, thus promoting the crystallinity of the acceptor,[74] however the resulting PSC FF and current density are only slightly increased by ~3% (**Table 2**) and are still significantly lower than in the symmetric-acceptor-based devices. These results suggest that enhancing the molecular crystallinity by simply increasing the weight percentage of the acceptor portion, introducing more π-electrons in the molecule, or enhancing the intramolecular planarity

cannot alter the intrinsic properties of these NFAs with asymmetric architectures. So, the function of the symmetric acceptor extra EG is not as simple as the extra π-electrons it provides or the greater molecular planarity. Instead, the additional EG of the symmetric acceptors appears to function primarily via the EG-EG π-π intermolecular stacking (*vide infra*). Further morphological analyses are described below.

SCLC mobility measurements on the **PM6:IDT-L4F** and **PM6:BTBO-L4F** BHJ blends indicate that both hole (~ 4.5 x 10^{-4} cm^{-2} v^{-1} s^{-1}) and electron (~ 9.0 x 10^{-4} cm^{-2} v^{-1} s^{-1}) mobilities are very similar (**Figure 2f-g** and **Table S7**), suggesting similar charge transport mechanisms. Interestingly, the hole mobilities in both the symmetric (8.8 - 9.7 x 10^{-4} cm^{-2} v^{-1} s^{-1}) and asymmetric (6.3 - 6.9 x 10^{-4} cm^{-2} v^{-1} s^{-1}) acceptor-based blends are also similar and close to that of the pristine **PM6** films, suggesting that holes are mainly transported through the BHJ donor domains, implying that the donor domain morphologies are not significantly impacted by the asymmetric acceptors. These results are consistent with the findings from TA and EPR measurements (*vide infra*). Furthermore, these results suggest that all blend film morphologies are similar and are dominated by the donor polymer instead of the acceptors. This is consistent with findings from AFM characterization (**SI Section S9**). However, note that the electron mobilities of the blends based on the asymmetric acceptors are two - three orders of magnitude lower than those of their symmetric counterparts (**SI Table S7, and Figure S32-33**). This suggests that the asymmetric acceptors are intrinsically less electron-conductive than the symmetric acceptors. Thus, to further evaluate the second reason noted above, it is important to understand why the additional electron-accepting EGs on the symmetric NFAs so dramatically increase the electron mobility versus the asymmetric acceptors. Thus, x-ray crystallography, AFM, TEM, and 2D-GIWAXS were utilized to probe the structural and morphological features of the pristine acceptors and blend films (*vide infra*).

Molecular packing and crystallographic analysis

It is well established that certain acceptor packing motifs in a BHJ can be detrimental to electron transport.[32,59,60] Thus, to further evaluate this possibility, we determined the single-crystal structures of the acceptors used in this study. To avoid terminology confusion,

in this study, **Br** stands for a bromine atom, **EG** stands for the difluorinated L2F end group, **D** stands for a thiophene, thioeno[3,2-n]thiophene, or methoxylthiophene unit, core stands for the **IDT** or **BTBO** aromatic core. The single-crystal structures of **T-IDT-L2F**, **MeOT-IDT-L2F**, **TT-IDT-L2F**, **IDT-L4F**, **Br-IDTT-L2F**, **IDTT-L4F** (a.k.a. **ITN-4F**)[75], **IDTT-4F** (a.k.a. **IT-4F**)[53], **Br-BTBO-L2F**, **T-BTBO-L2F**, **TT-BTBO-L2F**, and **BTBO-L4F**, are presented in **Figure 3**. Their synthetic protocols, and detailed crystallographic information are presented in **SI Section S2, S6** and **Table S3**.

Generally, **IDT/IDTT**-core-based acceptors have different packing motifs than the **BTBO**-core-based acceptors. A noteworthy stacking feature of the **IDT/IDTT** core-based acceptors is that they crystallize in 2D-lamellar networks with EG-EG stacking and negligible connectivity between lamellar layers (**Figure 3a**). Increasing the electron-donating characteristics of the asymmetric acceptors from a bromine atom to thiophene, thieno[3,2-b]thiophene or methoxylthiophene unit (**Br-IDT-L2F** → **T/TT/MeOT-IDT-L2F**), or increasing the π-conjugation length of the **IDT** core from one thiophene to thieno[3,2-b]thiophene (**Br-IDT-L2F** →**Br-IDTT-L2F**) can contract the interplanar separation between the lamellar layers (**Br-IDT- L2F**: 16.95 Å, **T-IDT-L2F**: 16.85 Å , **TT-IDT-L2F**: 16.30 Å, **Br-IDTT-L2F**: 12.37 Å, **MeOT-IDT-L2F**: 12.19 Å, **Figure 3a**). This suggests that the stronger electron-donating tendencies of the D unit or the core promotes more densely stacked networks. The shortest EG-EG stacking distance in the crystal structures of these materials

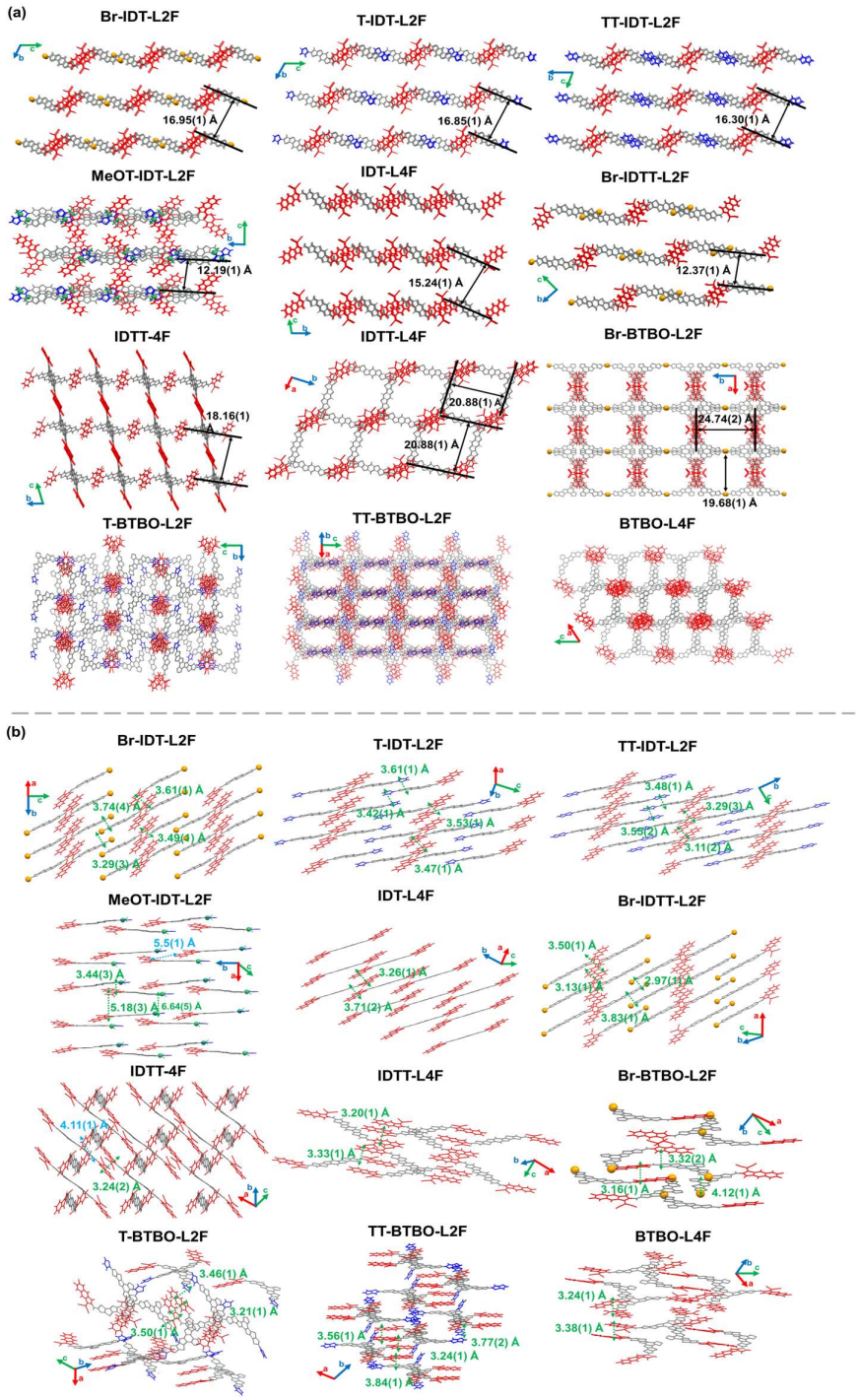

Figure 3. (a) Single-crystal structures and molecular packing viewed along the EG-EG stacking direction. Colors show the different components of the NFA molecules, red: L2F end groups; blue: thiophene or thieno[3,2-b]thiophene units; gray: core; green: methoxy groups; orange: bromine atoms. **(b)** Stacking distances of the present NFAs. Distances labeled in green are the shortest π-π interplanar distance. Distances labeled in blue are the EG-EG non-stacking coupling distances calculated from the plane of two nearest EGs. The single-crystal structures of **IDTT-L4F, IDTT-4F** and **BTBO-L4F** are taken from previous work (ref. 37, 26 and 10, copyright American Chemical Society, 2022).

is an essential stacking feature for efficient NFA electron transport. From the stackings of high-performance symmetric acceptors, **IDT-L4F**, **IDTT-L4F** (> 10% PCE)[75], and **BTBO-L4F**, it can be seen that only **IDTT-L4F** and **BTBO-L4F** crystals have a 3D-interpenetrating networks. Note however that **IDT-L4F** with similar PSC performance is has a 2D-lamellar crystal network, suggesting that a crystallographic 3D stacking network is not necessary overall efficient charge transport. The **IDTT-4F**(**IT-4F**) structure is unique among symmetric acceptors because it is stacking in two different orientations instead of one. In the horizontal orientation (**IDTT-4F** blue arrow **Figure 3b)**, the EG of **IDTT-4F** is strongly coupled with a nearby EG through a direct π-π stacking (17.1 meV computed, *vide infra*), but in the vertical orientation (**IDTT-4F**, green arrow **Figure 3b**), the EG is coupled with a nearby EG through a remote (> 4 Å) weak coupling (2.8 meV computed, *vide infra*), and there is no overlap between aromatic regions found. Interestingly, this remote non-overlapping EG-EG coupling is also found in the single-crystal structure of **MeOT-IDT-L2F** (5.50 Å, blue arrow **Figure 3b**). To the best of our knowledge, this is the first time that such remote non-overlapping EG-EG coupling has been reported in NFAs. Note that close EG-EG coupling in **MeOT-IDT-L2F** exists only as dimers, and there is a lack of continuous EG-EG stacking between the dimers of **MeOT-IDT-L2F** in its crystal network. So, when **MeOT-IDT-L2F** is blended with the donor polymer, the crystallinity of the blend film is enhanced but nevertheless exhibits low OSC performance as in other asymmetric IDT-core acceptors(*vide infra*).

Regarding symmetric **IDT**/**IDTT**-core-based acceptors, note that they all exhibit surprising uniformity, such that the EGs at each side of the symmetric molecule are closely π-π stacked with an EG from a nearby molecule (2-D continuous EG- EG stacking). In contrast, in the asymmetric **IDT/IDTT**-core based acceptors, the Br atom and the D unit stack with the Br atom and D unit of a nearby molecule (1D continuous D-D stacking, **Figure 3b**), and the EG of the **IDT/IDTT**-based asymmetric acceptor stacks with another EG of the nearby molecule (1D continuous EG-EG stacking). Thus, there is no EG-Br/D/core intermolecular stacking found in the IDT/IDTT-based acceptors. The **BTBO-**core-based acceptor **BTBO-L4F** is similar to **IDT-L4F** and **IDTT-L4F**, with continuous EG-

EG stacking at each side of the molecule. However, in the **BTBO**-core-based asymmetric acceptors, the situation is more complicated. The **Br-BTBO-L2F** acceptor has a similar stacking pattern to that in the IDT/IDITT-based asymmetric acceptors, with a continuous EG-EG stacking on one side of the molecule and a continuous D-D stacking on the other. Also, there is no EG-Br/D/core stacking found in **Br-BTBO-L2F** crystal network. For the **T-BTBO-L2F** and **TT-BOBO-L2F** NFAs, the situation is different. There are no continuous EG-EG and D-D stackings, instead, they exhibit a 'sandwich-style' EG-D/core capping motif, where the EG-EG stacking is capped from both the top and the bottom by a BTBO-core (3.84 Å in **TT-BTBO-L2F**) and a D unit (3.46 Å in **T-BTBO-L2F**).

Combining the findings from the single-crystal structural analysis, it appears that the formation of continuous 2D EG-EG stacking is essential for a high-performance acceptor. However, it is unclear why the D-D stacking and the sandwich-style capped EG-EG stacking cannot function as in the common continuous EG-EG stacking of the high-performance symmetric acceptors. To address this point, theoretical computations were next carried out to explore the electronic structures of these acceptors (*vide infra*).

Computational studies

Quantum mechanical calculations with DFT were conducted to investigate the electronic structure and transport properties of these asymmetric acceptors. Three major findings were extracted from these calculations: 1) The asymmetric NFAs have lower vertical ionization energies (IEs) and vertical electron affinities (EAs) than their symmetric counterparts (**Figure 1h-i)**. A lower IE indicates the asymmetric NFAs are more easily ionized to the excited state upon irradiation and should aid exciton separation at the donor-acceptor interface. However, a lower EA means it is more difficult to stabilize electrons in the NFA backbone and thus increases the likelihood of termination events such as bimolecular recombination and electron loss. 2) The asymmetric NFAs have lower electron-IREs than the symmetric NFAs and are therefore more stable towards charge transport. In turn, the symmetric NFA excitons require less to be energy separated at the D-A interface which is therefore beneficial to the exciton separation process. This is in good agreement with the photovoltaic (PV) results and the lower EAs of the asymmetric

acceptors. The hole-IRE is higher in asymmetric acceptors than in symmetric acceptors, which indicates that hole transport is less stable. This is consistent with the findings from transient absorption (*vide infra*), where the BHJ asymmetric acceptor hole transfer process is slower than for the symmetric acceptors. 3) The electronic coupling (**SI Figure S76-83, Table S17-24**) indicates that the symmetric **IDT-L4F** has a moderate coupling strength (68.5 meV) in two directions, but the asymmetric IDT-core acceptor has only one very strong coupling (EG··EG stacking, > 110 meV); the D(Br)···D(Br) stacking is weak and barely coupled (< 1 meV), so electrons cannot be transported through D-D stacking. The single strong coupling suggests the asymmetric NFA has a favored stacking in the solid state that inhibits charge transport across a crystalline domain, unlike the symmetric NFA. The electronic coupling in **BTBO-L4F** is similar to that of **IDT-L4F**, where the EG at each side of the molecule has moderate coupling strength.

For the asymmetric BTBO-core-based acceptors, they not only have large EG··EG coupling (60-70 meV), but also possess a weak EG··D/core coupling due to the sandwich-style capped EG··D/core stacking (**T-BTBO-L2F**: AE = 12.1 meV, **TT-BTBO-L2**: AD = 20.2 meV). Interestingly, even though the EG··D/core stacking in **T/TT-BTBO-L2F** exhibits a moderate coupling strength, the LUMO of the asymmetric acceptors is still mainly localized on the EG unit, and the HOMO is mostly distributed through the core and the D unit as a whole. Thus, there is no intermolecular LUMO-LUMO overlap between the EG and the core/D unit, which is important for electron hopping. Thus, the EG can couple with the nearby core and D units, but essentially cannot form an efficient electron transport channel.

Morphological characterization

To understand how (a)symmetry impacts the film morphology and crystallinity of the BHJ films, the donor–acceptor blend films were characterized with AFM, TEM, and 2D-GIWAXS. The surface roughness of blend films was first probed by AFM (**SI** section **S9**). In the neat acceptor films, the asymmetric acceptors all exhibit smoother surfaces than their symmetric counterparts, suggesting a weaker crystallinity of the asymmetric acceptors which is consistent with the GIWAXS analysis (*vide infra*). Interestingly, the phase images show that all **PM6** blend films exhibit nano-fibrillar surface morphologies,

suggesting that the donor determines the film morphology. TEM images exhibit a similar tendency as the AFM images, where the symmetric acceptors-based blends have a rougher surface and more evident phase separation and aggregation, while the asymmetric acceptor-based blends are instead more uniform and smoother **(SI** section **S10).** The miscibility between the acceptors and the donor polymer can also be qualitatively estimated from the AFM and TEM images, in which no over-sized aggregation in the blend films of both symmetric and asymmetric acceptors is observed, suggesting that the

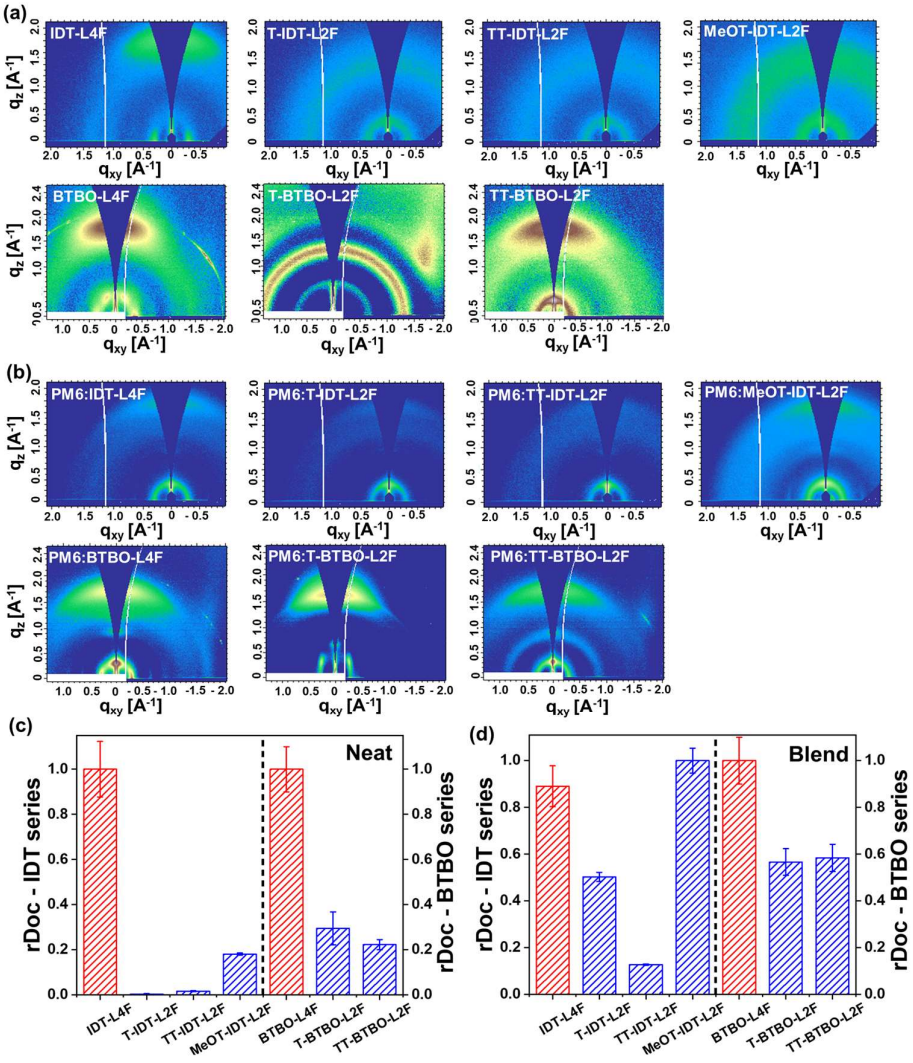

Figure 4. 2-D GIWAXS patterns of the indicated (a) neat films and (b) blend films. (c)-(d) Plot of the relative degree of crystallinity (rDoC) of the blends obtained by integrating the pole figures. The rDoC for neat and blend samples for a certain acceptor type were obtained by normalizing the intensities to different samples and should not be cross compared. Error bars in (c) and (d) were obtained from the standard deviation in sample volume (thickness and width) measurements.

symmetry of the acceptors does not significantly alter the miscibility of the acceptors.

The 2-D GIWAXS images of the pristine polymer donor and NFA component and blend films are shown in **Figures 4a** and **4b,** respectively. The 1-D linecuts for the polymer donor PM6, IDT and BTBO series of molecular acceptors are shown in **Figures S34** and **S35,** respectively. Due to different packing motifs and the structure factors of the materials involved we will restrict our discussion to the low-q lamellar stacking peak and the high-q π-π stacking peak in the data to compare the ordering in the different materials. For both the symmetric acceptors, the notable features in the PM data are a lamellar stacking peaks at 0.29 $Å^{-1}$, 0.64 $Å^{-1}$ and π-π stacking peak at 1.7 $Å^{-1}$. In the data from the **BTBO-L4F** and **IDT-L4F** samples a strong in-plane (IP) lamellar stacking peak in the q-range 0.3 $Å^{-1}$ to

The asymmetric IDT acceptors (**MeOT-IDT-L2F**, **TT-IDT-L2F**, and **T-IDT-L2F**) show much broader and weaker lamellar stacking peaks centered at 0.35 $Å^{-1}$ and a π-π stacking peak at 1.68 $Å^{-1}$ is observed suggesting a higher degree of disorder in the samples. The data from the blend samples with the asymmetric acceptors have a lamellar stacking peak at 0.30 $Å^{-1}$ and a π-π stacking peak around 1.72 $Å^{-1}$ that matches with that of pristine **PM6** Therefore, the diffraction in the blend samples prepared with the asymmetric acceptors most likely arises from **PM6** ordering and is in excellent agreement with observations from AFM. On the hand other, the peak positions observed for the blend with the symmetric acceptor (**PM6**:**IDT-L4F**) suggest that they probably arise from **PM6** as well as **IDT-L4F** ordering. For the **BTBO** acceptor neat materials, the **BTBO-L4F** sample shows a low-q lamellar reflection at 0.36 $Å^{-1}$ and a high-q π-π feature at 1.77 $Å^{-1}$. The corresponding diffraction peaks appear at 0.31 $Å^{-1}$ and 1.73 $Å^{-1}$ for the **TT-BTBO-L2F** sample. However, the peaks occur at considerably different positions (0.69 $Å^{-1}$ and 1.92 $Å^{-1}$) for the neat **T-BTBO-L2F** film suggesting a different packing motif in that material, which agrees with the single-crystal XRD data. Similarly, the low-q and high-q peak locations in the **PM6:BTBO-L4F** and **PM6:TT-BTBO-L2F** blend data are similar to corresponding peaks in the neat polymer and acceptor data. In the **PM6:T-BTBO-L2F** blend, in addition to the **PM6** lamellar stacking peak at 0.28 $Å^{-1}$, another low-q peak at 0.44 $Å^{-1}$ is observed which indicates formation of a **T-BTBO-L2F** polymorph. The π-π stacking reflection is also found to be at a

different location (1.62 $Å^{-1}$) compared to the other two **BTBO** blends. The match between peak positions in the blend data with that of the pure polymer combined with the fact that **PM6** fibrils are observed in the AFM data from the blends argue for the presence of ordered **PM6** regions in the films. Assuming similar structure factors between neat and blend samples for a particular family of acceptors, the relative degree of crystallinity (rDoC) obtained by integrating geometry corrected pole figures from π-π stacking peak in the **IDT** and **BTBO** neat and blend film data are shown in **Figures 4c** and **4d**, respectively.

For both acceptor families the relative degree of crystallinity in the pristine films is found to be maximum for the symmetric acceptor. Similar trends are found in the blends except for the **PM6:MeOT-IDT-L2F** blend. However, the match between peak positions for the blend and pure polymer suggests that the crystallinity in that sample can be mostly attributed to **PM6** ordering. In the other blend samples, the crystallinity arises from a combination of polymer and acceptor ordering. The average molecular orientation (*S*) in the neat and blend samples was calculated from the lamellar stacking peak near q = 0.3 $Å^{-1}$ (see SI for details). S>0 and S<0 imply predominantly edge-on and face-on orientation with respect to the substrate, respectively, whereas *S*=0 implies a perfectly random orientation. For the both **IDT** and **BTBO** neat films, the lower magnitude of *S* suggests a more random stacking of acceptor molecules in those films. All the **IDT** blend samples have a preferential edge-on orientation. The *S* value for the asymmetric acceptor blends is closer to that of neat **PM6** which further confirms that the ordering in those samples arises from the polymer donor. The **BTBO** blends on the other hand have a mildly preferential face-on ordering and *S* is found to be lower for the **PM6:T-BTBO-L2F** blend suggesting a more random molecular orientation. The GIWAXS results therefore show that the π-π stacking as well as the orientation of the asymmetric acceptor molecules in the neat and blend samples is overall weaker than in their symmetric counterparts. A similar crystallite coherence length (CCL) of ≈ 3 nm obtained from Scherrer analysis of the GIWAXS data from the BTBO neat and blend films suggesting a high degree of disorder dominates the coherence length and hinders the determination of crystallite size in those samples.[76]

Femto/nano-second transient absorption spectroscopy, time-resolved electron

paramagnetic resonance spectroscopy, and impedance analysis

The dynamics of excitons and free carriers in the present BHJ films were probed using femtosecond (fsTA) and nanosecond (nsTA) transient absorption spectroscopies (**Figures 5** and **S39-S63**, **Tables S10-S13**). An excitation wavelength of 750 nm is used to selectively excite the acceptor domains in the blends since PM6 donor domains do not absorb in this region of the spectrum. The selective photoexcitation of the acceptor domains enables generation and diffusion of excitons in the acceptor and hole transfer from the acceptor to the donor, while eliminating generation and diffusion of excitons in the donor and electron transfer from the donor to the acceptor. The fsTA and nsTA results are compared across the series of blends containing either **IDT** or **BTBO**, as the similar core constituents lead to similar electronic structures within each series.

After photoexcitation, ultrafast hole transfer from the acceptor to the donor within the instrument response time of ~300 fs in fsTA is observed for all blends, as indicated by the peak corresponding to the ground-state bleach (GSB) of the donor at ~625 nm (**Figure 5a**). In the IDT series, hole transfer is faster in **PM6:IDT-L4F** (~500 fs) than in **PM6:TT-IDT-L2F** (~3 ps) and **PM6:T-IDT-L2F** (~30 ps), as shown in **Figure 5b.** Similarly, in the **BTBO** series, hole transfer is faster in **PM6:BTBO-L4F** (< 100 fs) than in **PM6:T-BTBO-L2F** (~500 fs) and **PM6:TT-BTBO-L2F** (~500 fs), as shown in **Figure 5c**. The faster hole transfer in symmetric acceptor sets (**PM6:IDT-L4F** and **PM6:BTBO-L4F**) is consistent with the higher PCE in these blends. The slower hole transfer in asymmetric acceptor set, **PM6:T-IDT-L2F**, **PM6:TT-IDT-L2F**, **PM6:T-BTBO-L2F**, and **PM6:TT-BTBO-L2F** may be due to larger acceptor domains or slower exciton diffusion in the acceptor domains. Given that the blend crystallinity of asymmetric acceptor sets is significantly smaller than the symmetric acceptor sets calculated from the GIWAXS rDOC analysis, it is reasonable that the slower hole transfer is indeed caused by the slower exciton diffusion. This is also in good agreement with findings of the DFT calculations in which the asymmetric acceptors exhibit much greater hole-IRE than in the symmetric acceptors. Because the overall device performance depends on a sequence of efficient charge transfer events, ultrafast hole transfer is a necessary condition to ensure that enough of the excited state population is

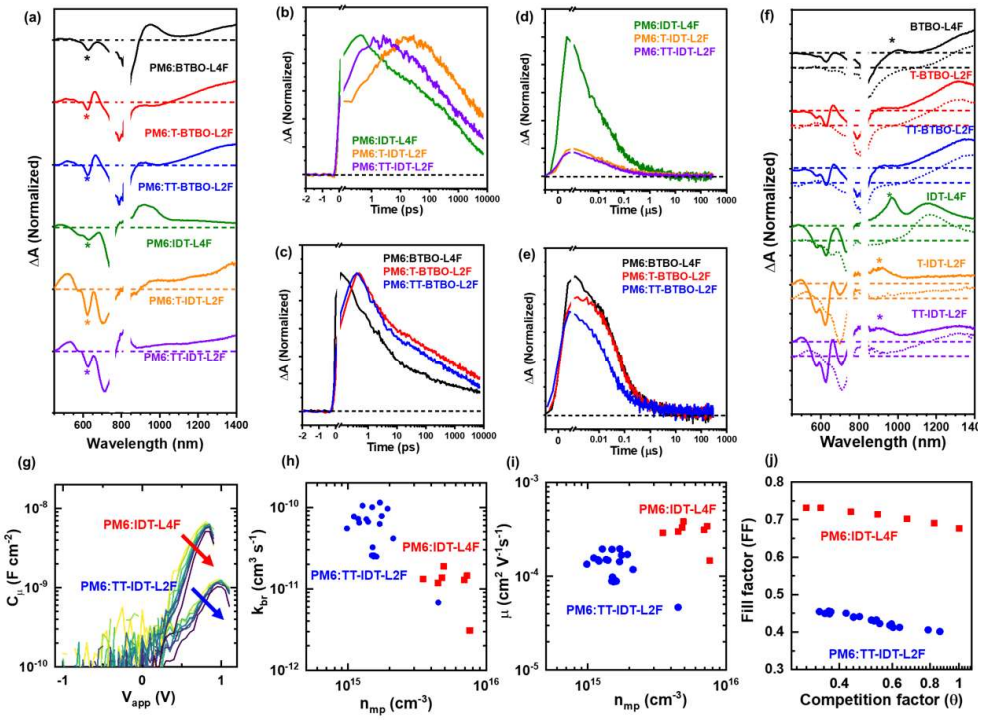

Figure 5. fs/na Transient Absorption (a) Optical absorption spectra of BHJ blend films at a delay time of 200 fs after photoexcitation, with the donor GSB at ≈625 nm indicated by *. fsTA kinetics of the GSB of the donor for the blend films in the **(b) IDT** and **(c) BTBO** series. nsTA kinetics of the GSB of the donor for the blend films in the **(d) IDT** and **(e) BTBO** series. **(f)** Absorption spectra of the blend (solid) and neat (dashed) films at a delay time of 20 ps after photoexcitation, with the peak present in blend films but not in neat films indicated by *. Data in (a), (b), (c), and (f) are normalized by the maximum intensity whereas data in (d) and (e) are normalized by the number of absorbed photons at the excitation wavelength of 750 nm, which is performed by dividing the transient absorption intensity by the quantity ($1-10^{-A}$) for each blend film, where *A* is the absorbance at 750 nm. **Impedance based analysis**. **(g)** Chemical capacitance (C_μ) versus applied voltage (V_{app}) for IDT-L4F and TT-IDT-L2f cells at varying intensities from 1 Sun to 0.3 Sun (top to bottom as shown by arrows). **(h)** Plot of bimolecular recombination coefficient (k_{br}) as a function of carrier density at maximum power point (nmp) derived from the IPDA analysis of the indicated IDT-L4F and TT-IDT-L2F PSCs. **(i)** Mobility (μ) versus nmp from the same cells. **(j)** Fill factor versus competition factor showing different trade-off relation in the indicated IDT-L4F and TT-IDT-L2F PSCs.

converted into charge carriers that will then be collected and converted to meaningful work.[31,77-82]

The (singlet) Frenkel exciton peaks of the acceptors are readily assigned using the early-time fsTA spectra of each neat blend (**Figure S45-S50**), which reveal excited-state absorption bands in the 1100-1400 nm range. Features in Figure 5f denoted by asterisks

are assigned to charge carriers in the blends, typically peaking around 900-1000 nm.[83-85] The charge carriers could either be polarons or free carriers—since these two species are comprised of the same ionic states, their spectra are similar except for subtle shifts associated with the exciton binding energy. The triplet excitons of ITIC and related non-fullerene acceptors typically show excited-state absorption features around 1400 nm[86], though these can be difficult to disentangle from the singlet excitons given the observed spectra of the neat acceptor films at early time before spin evolution can proceed.

To compare the relative quantum yields of hole transfer from acceptor to donor within blend films, the kinetics of the donor GSB in each blend is normalized by the number of absorbed photons at the excitation wavelength. In the IDT series (**Figure 5d**), the yield of hole transfer in **PM6:IDT-L4F** 5x larger than that in **PM6:TT-IDT-L2F** and **PM6:T-IDT-L2F** at 1 ns, and remains a factor of at least 3x larger as time increases to 1 μs. In the **BTBO** series (**Figure 5e**), the yield of hole transfer in **PM6:BTBO-L4F** is 1.2x and 1.4x larger than in **PM6:T-BTBO-L2F** and **PM6:TT-BTBO-L2F**, respectively, at 1 ns. Beyond 20 ns, yields of hole transfer in **PM6:BTBO-L4F** and **PM6:T-BTBO-L2F** blends are nearly identical, whereas, as time increases to 100 ns, the yield of hole transfer in **PM6:BTBO-L4F** becomes 2x larger than in **PM6:TT-BTBO-L2F**. The larger yield of hole transfer in **PM6:IDT-L4F** and **PM6:BTBO-L4F** is consistent with the higher PCEs in these blends; however, given the vast difference in PCEs within the **BTBO** series, a larger difference in yield of hole transfer is expected.

The transient spectra of the blend and neat films are next compared to further understand the origin of the GSB of the donor in **Figure 5d-e**. Transient spectra of **PM6:BTBO-L4F**, **PM6:IDT-L4F**, **PM6:T-IDT-L2F**, and **PM6:TT-IDT-L2F** exhibit an additional absorptive peak between 900 and 1000 nm that is not present in neat films, as shown in **Figure 5f** and **S60**. This additional peak is attributed to either weakly-bound electron-hole pairs (i.e., polarons) or the cation peak of the donor (i.e., free charge carriers),[87,88] each of which contributes to the intensity of the GSB of the donor and contributes to OPV photocurrent.[89] The kinetics of the charge carrier peaks are compared in **Figure S63-64**. **PM6:T-BTBO-L2F** and **PM6:TT-BTBO-L2F** do not show an additional

peak between 900 and 1000 nm, indicating that the yield of polarons or free charge carriers is relatively low. In addition, time-resolved electron paramagnetic resonance (EPR) spectroscopy (**Figure S63-64**) indicates that triplet excitons are detected in **PM6:T-BTBO-L2F** and **PM6:TT-BTBO-L2F**, but not in the other blends.

These results lead to the conclusion that the donor GSBs in **PM6:T-BTBO-L2F** and **PM6:TT-BTBO-L2F** in **Figure 5e** contain a larger contribution from the strongly bound charge-transfer state or triplet excitons, rather than from polarons or free carriers versus that in **PM6:BTBO-L4F**. Therefore, while the hole transfer yield in **PM6:T-BTBO-L2F** and **PM6:TT-BTBO-L2F** is on the same order as that in **PM6:BTBO-L4F**, the yield of polarons or free carriers that can contribute to photocurrent in OPVs is relatively low in the two asymmetric acceptor systems because of the combination of inefficient separation of the strongly bound charge-transfer state and non-radiative decay via the triplet state.

The role of NFA (a)symmetry in photocarrier dynamics was next investigated by in situ integrated photocurrent device analysis (IPDA) in solar cells, using the protocols outlined earlier.[33,69,77,90,91] IPDA enables an in situ determination of the bimolecular recombination rate constant (kbr) and carrier mobilities (μ) that is more related to the device performance than would be accessible from a power dependence study by TA spectroscopy, especially as the TA signals are not very strong at longer times where bimolecular recombination will dominate.Three NFA molecules are considered, **IDT-L4F**, **TT-IDT-L2F**, and **T-IDT-L2F** since these variations yield operational PSCs with a large and monotonic variation in PCE values with the degree of symmetry in the molecular structure (**Table 1**). For IPDA, photocurrent (J_{PC}) and impedance measurements were conducted on cells under varying illumination intensity inside an inert N_2 glove box (**SI Section S16**). An onset of reverse saturation current is clearly visible in **IDT-L4F** in contrast to **TT-IDT-L2F** and **T-IDT-L2F** cells that show a lack of current saturation (**SI Figure S84**). The peak chemical capacitance (C_μ) of **IDT-L4F** cells is 5x larger than that in **TT-IDT-L2F** cells and the peak voltage is lower by ~200 mV, in agreement with observed V_{OC} values (**Figure 5g, Table 2**) and consistent with the quantum yields observed in the transient absorption discussed above. Note that the chemical capacitance of **T-IDT-L2F** could not be extracted due to the failure to fit a

simple RC model to impedance spectra thus precluding extraction of device parameters. Self-consistent calculation of carrier density at the maximum power point (n_{mp}) shows roughly a 5x larger n_{mp} in **IDT-L4F** than **TT-IDT-L2F** cells (**Figure 5h**). Furthermore, **IDT-L4F** cells also show a lower bimolecular recombination coefficient (k_{br}) and slightly increased carrier mobility (μ) than **TT-IDT-L2F** cells. The combined effect of improved charge recombination and extraction processes in **DT-L4F** can be more clearly seen in the competition factor ($\theta \sim k_{br}/(\mu)^2$) that has been shown to scale with fill factor (FF) in a wider class of organic photovoltaics (**Figure 5i**).[91,92] Interestingly, while the FF scales well with θ within the **IDT-L4F** and **TT-IDT-L2F** cells, their data are shifted vertically without following the same tradeoff relation. Thus, a significantly lower FF in the **TT-IDT-L2F** cells is not simply due to a dominance of bimolecular recombination even though the increased value of k_{br} is expected to contribute to some reduction in the performance. Instead, such deviation from the tradeoff relation points to fundamental changes in the stacking motifs of the NFA and resulting morphology differences. Previously, similar deviations in the FF-θ tradeoff and dramatic reduction in PCE to 2.6% were seen in the case of co-crystal formation in **PBTATBT-2f:Y6** solar cells where decreased fluorination in the donor polymer disrupted NFA motifs.[93] Indeed, simulated molecular packing of **TT-IDT-L2F** molecules in single crystal points to the alignment of the core and end groups that could disrupt the formation of nanocrystals and the desired mixing with the donor polymer for an efficient bulk heterojunction. Therefore, IPDA concludes that the symmetry of NFA molecules is critical to the formation of donor: NFA heterojunctions with well-connected domains for electron and hole transport.

Conclusions and Outlook

Combining the findings from the photovoltaic measurements, charge carrier mobility, single-crystal structure analyses, morphological analyses, DFT studies, time-resolved optical spectroscopy, and impedance-based analysis, we propose the following symmetry guidelines in PSC NFAs: 1) The acceptor symmetry impacts the acceptor optical absorption spectra and cross-sections. Acceptors with dual EG motifs exhibit stronger absorbance, but also a red-shifted absorption profile. 2) Symmetric acceptor-based PSCs

exhibit superior power conversion performance; this is ascribed to their larger electron mobility and more balanced charge carrier mobilities. 3) Asymmetric acceptors exhibit reduced crystallinity versus symmetric acceptors, which is mainly due to the asymmetric acceptors possessing fewer π-electrons and the D unit not effectively stacking with nearby molecules in the crystal structure. Introducing an S-O conformational lock between the D unit and the core to limit the rotation of the D unit can significantly boost the overall crystallinity of the asymmetric acceptor in neat and blend films. 4) A 2D/3D stacking network is beneficial to exciton and electron transport in the acceptor crystalline domains. Increasing the intramolecular D-A coupling strength can effectively reduce the lamella interplanar distance in **IDT**-core based acceptors, facilitating formation of 3D stacking networks in the single-crystals. 5） Given similar values of vertical IR and IRE in the symmetric and asymmetric acceptors, as calculated from DFT, the symmetric architecture (A-D-A, and A-DA'D-A) of an NFA is not detrimental to efficient exciton generation and separation in the active layer. NFAs with asymmetric architectures (D-A, D-D-A, DA'D-A, and D-DA'D-A architecture) can still be efficiently ionized (excited) to generate and separate excitons with low energy loss at the donor-acceptor interface. However, the symmetric architecture is essential to the intramolecular exciton transport. Due to the slower hole transfer, it is more challenging for acceptors with asymmetric architectures to transport excitons, resulting in higher bimolecular recombination coefficients and more severe non-radiative decay via triplet states. 6) Due to a lack of effective FMO overlap, the stacking between the D unit (D-D stacking, Br-Br stacking) and the EG-D/core stacking hampers exciton transport so fewer excitons can reach the donor-acceptor interface, resulting in a much lower current density in asymmetric acceptor-based devices.

Overall, this work provides a systematic study of the fundamental design rules favoring symmetric architectures in non-fullerene acceptors and answers the questions of why and how the EG-EG π-π stackings on both sides of the acceptor molecules are essential for efficient exciton transport within the acceptor crystalline domains. This work provides both practical and theoretical guidelines for the future development of high-performance non-fullerene acceptors in organic photovoltaics.

Conflicts of interest

Authors declare no conflicts of interest.

Corresponding Authors

Vinod K. Sangwan − Department of Materials Science and Engineering, Northwestern University, Evanston, Illinois 60208, United States; orcid.org/0000-0002-5623-5285;
Email: vinod.sangwan@northwestern.edu

Dean M. DeLongchamp − Material Measurement Laboratory, National Institute of Standards and Technology, Gaithersburg, Maryland 20899, United States;
Email: dean.delongchamp@nist.gov

Kevin L. Kohlstedt − Department of Chemistry, the Center for Light Energy Activated Redox Processes (LEAP), and the Materials Research Center (MRC), Northwestern University, Evanston, Illinois 60208, United States; orcid.org/0000- 0001-8045-0930; Email: kkohlstedt@northwestern.edu

Michael R. Wasielewski − Department of Chemistry, the Center for Light Energy Activated Redox Processes (LEAP), and the Materials Research Center (MRC), Northwestern University, Evanston, Illinois 60208, United States;orcid.org/0000-0003-2920-5440; Email: mwasielewski@northwestern.edu

Mark C. Hersam − Department of Materials Science and Engineering, Northwestern University, Evanston, Illinois 60208, United States; Department of Chemistry, the Center for Light Energy Activated Redox Processes (LEAP), and the Materials Research Center (MRC), Northwestern University, Evanston, Illinois 60208, United States; orcid.org/0000-0003-4120-1426;
Email: m-hersam@northwestern.edu

George C. Schatz − Department of Chemistry, the Center for Light Energy Activated Redox Processes (LEAP), Northwestern University, Evanston, Illinois 60208, United States; orcid.org/0000- 0001-5837-4740;
Email: g-schatz@northwestern.edu

Yinhua Zhou – Wuhan National Laboratory for Optoelectronics, Huazhong University of Science and Technology, Wuhan 430074, China.
Email: yh_zhou@hust.edu.cn

Antonio Facchetti − Department of Chemistry, the Center for Light Energy Activated Redox Processes (LEAP), and the Materials Research Center (MRC), Northwestern University, Evanston, Illinois 60208, United States; Flexterra Corporation, Skokie, Illinois 60077, United States; orcid.org/0000-0002-8175-7958;
Email: a-facchetti@northwestern.edu

Tobin J. Marks − Department of Chemistry, the Center for Light Energy Activated Redox Processes (LEAP), and the Materials Research Center (MRC), Northwestern University, Evanston, Illinois 60208, United States; Department of Materials Science and Engineering, Northwestern University, Evanston, Illinois 60208, United States; orcid.org/0000-0001-8771-0141;
Email: t-marks@northwestern.edu

Authors

Guoping Li − Department of Chemistry, and the Materials Research Center (MRC), Northwestern University, Evanston, Illinois 60208, United States; orcid.org/0000-0002-8193-9639

Fei Qin – Wuhan National Laboratory for Optoelectronics, Huazhong University of Science and Technology, Wuhan 430074, China. And Department of Chemistry, Northwestern University, Evanston, Illinois 60208, United States; orcid.org/0000-0002-8193-9639

Robert M. Jacobberger − Department of Chemistry, and the Materials Research Center (MRC), Northwestern University, Evanston, Illinois 60208, United States;

Subhrangsu Mukherjee − Material Measurement Laboratory, National Institute of Standards and Technology, Gaithersburg, Maryland 20899, United States; orcid.org/0000-0002-5479-3750

Leighton O. Jones − Department of Chemistry, Northwestern University, Evanston, Illinois 60208, United States; orcid.org/0000- 0001-6657-2632

Ryan M. Young − Department of Chemistry, and the Materials Research Center (MRC), Northwestern University, Evanston, Illinois 60208, United States;

Robert M. Pankow − Department of Chemistry, and the Materials Research Center (MRC), Northwestern University, Evanston, Illinois 60208, United States;

Brendan Kerwin − Department of Chemistry, and the Materials Research Center (MRC), Northwestern University, Evanston, Illinois 60208, United States;

Ding Zheng − Department of Chemistry, and the Materials Research Center (MRC), Northwestern University, Evanston, Illinois 60208, United States;

Liang-Wen Feng - Key Laboratory of Green Chemistry &Technology, Ministry of Education, College of Chemistry, Sichuan University, Chengdu 610065, China;

Author Contributions

G.L. and F.Q. contributed equally. G. L., F. Q. , A. F. and T. J. M. conceived the idea. G. L. synthesized the acceptors used in this study, characterized the physical properties (UV, CV, TEM), and grew the single crystals. F. Q. fabricated and measured the solar cell devices and conducted SCLC measurements. F. Q. and Y. Z. analyzed the data measured from the solar cell devices. R. M. P., L.Q.F., S. M. and D. M. D conducted the GIWAXS measurement and the data analysis. L. O. J., K. L. K and G. C. S. performed the DFT computation. R. M. J., R. M. Y., and M. R. W. conducted the fs/ns TA measurement and the data analysis. D. Z. conducted the UPS measurement. B.P.K. conducted the AFM measurement; V. K. S. and M. C. H. conducted the IPDA measurement and the data

analysis. G. L. performed single-crystal structure analysis. All authors analysed the results and prepared the paper.

Acknowledgements

This work was supported by U.S. Office of Naval Research Contract #N00014-20-1-2116 (G.L.: material synthesis and characterizations; F. Q.: photovoltaic device fabrication and measurement; D.Z.; R.M.P.: GIWAXS data collection) and by the U.S. Department of Commerce, National Institute of Standards and Technology as part of the Center for Hierarchical Materials Design Award #- 70NANB19H005. (S.M.; L.Q.F.; D.M.D: GIWAXS measurement and analysis), and the Northwestern University Materials Research Science and Engineering Center Award NSF DMR-1720139 (V.K.S.: impedance measurements) and the Qatar National Research Foundation grant NPRP12S-0304-190227/02-484761 (GL). Theory development (KLK, LOJ, GCS) was supported by NSF Grant CHE-2055565. Transient optical spectroscopy was supported by the U. S. Department of Energy, Office of Science, Office of Basic Energy Sciences under Award DE-FG02-99ER14999 (MRW). This work made use of the EPIC, BioCryo, Keck-II, and/or SPID facilities of Northwestern's NUANCE Center, which received support from the Soft and Hybrid Nanotechnology Experimental (SHyNE) Resource (NSFECCS-1542205) and Northwestern University Materials Research Science and Engineering Center (NSF DMR-1720139). We thank the Integrated Molecular Structure Education and Research Center (IMSERC) for characterization facilities supported by Northwestern U.S. National Science Foundation (NSF) under NSF CHE1048773, Soft and Hybrid Nanotechnology Experimental (SHyNE) Resource (NSF NNCI-1542205), the State of Illinois, and International Institute for Nanotechnology (IIN). This work was supported by the Department of Energy under contract no. DE-AC02-05CH11231 and used resources at beamline 8-ID-E of the Advanced Photon Source, a U.S. Department of Energy (DOE) Office of Science User Facility operated for the DOE Office of Science by Argonne National Laboratory under Contract No. DE-AC02-06CH11357. This research used beamlines 7-ID-1 (SST-1) and 11-BM (CMS) of the National Synchrotron Light Source II, a U.S. Department of Energy (DOE) Office of Science User Facility operated for the DOE Office of Science by Brookhaven

National Laboratory under Contract No. DE-SC0012704.This work (IPDA) made use of the MatCI Facility which receives support from the MRSEC Program (NSF DMR-1720139) of the Materials Research Center at Northwestern University. The theory research was also supported in part through the computational resources and staff contributions provided for the Quest high performance computing facility at Northwestern University which is jointly supported by the Office of the Provost, the Office for Research, and Northwestern University Information Technology. This work made use of the GIANTFab core facility at Northwestern University. GIANTFab is supported by the Institute for Sustainability and Energy at Northwestern and the Office of the Vice President for Research at Northwestern. Xiaoying Xing (Northwestern University) was acknowledged for her help in designing the TOC figure. Note that certain commercial equipment, instruments, or materials are identified in this paper to specify the experimental procedure adequately. Such identification is not intended to imply recommendation or endorsement by NIST, nor is it intended to imply that the materials or equipment identified are necessarily the best available for the purpose.

REFERENCES

1. Zhang, G.C., Lin, F.R., Qi, F., Heumuller, T., Distler, A., Egelhaaf, H.J., Li, N., Chow, P.C.Y., Brabec, C.J., Jen, A.K.Y., and Yip, H.L. (2022). Renewed Prospects for Organic Photovoltaics. Chem. Rev. 10.1021/acs.chemrev.1c00955.
2. Li, Y., Huang, X., Ding, K., Sheriff, H.K.M., Ye, L., Liu, H., Li, C.-Z., Ade, H., and Forrest, S.R. (2021). Non-fullerene acceptor organic photovoltaics with intrinsic operational lifetimes over 30 years. Nat. Commun. *12*, 5419. 10.1038/s41467-021-25718-w.
3. Zhang, G., Ning, H., Chen, H., Jiang, Q., Jiang, J., Han, P., Dang, L., Xu, M., Shao, M., He, F., and Wu, Q. (2021). Naphthalenothiophene imide-based polymer exhibiting over 17% efficiency. Joule *5*, 931-944. 10.1016/j.joule.2021.02.003.
4. Zhang, J.Q., Tan, H.S., Guo, X.G., Facchetti, A., and Yan, H. (2018). Material insights and challenges for non-fullerene organic solar cells based on small molecular acceptors. Nat. Energy *3*, 720-731. 10.1038/s41560-018-0181-5.
5. Bernardo, G., Lopes, T., Lidzey, D.G., and Mendes, A. (2021). Progress in Upscaling Organic Photovoltaic Devices. Adv. Energy Mater. *11*, 2100342. https://doi.org/10.1002/aenm.202100342.
6. Schopp, N., Akhtanova, G., Panoy, P., Arbuz, A., Chae, S., Yi, A., Kim, H.J., Promarak, V., Nguyen, T.-Q., and Brus, V.V. (2022). Unraveling Device Physics of Dilute-Donor Narrow-Bandgap Organic Solar Cells with Highly Transparent Active Layers. Adv. Mater. *34*, 2203796. https://doi.org/10.1002/adma.202203796.
7. Jiang, Z., Wang, F., Fukuda, K., Karki, A., Huang, W., Yu, K., Yokota, T., Tajima, K., Nguyen,

T.-Q., and Someya, T. (2020). Highly efficient organic photovoltaics with enhanced stability through the formation of doping-induced stable interfaces. Proc. Natl. Acad. Sci. U.S.A. *117*, 6391-6397. 10.1073/pnas.1919769117.

8. Wang, G., Huang, W., Eastham, N.D., Fabiano, S., Manley, E.F., Zeng, L., Wang, B., Zhang, X., Chen, Z., Li, R., et al. (2017). Aggregation control in natural brush-printed conjugated polymer films and implications for enhancing charge transport. Proc. Natl. Acad. Sci. U.S.A. *114*, E10066-E10073. 10.1073/pnas.1713634114.
9. Qin, F., Wang, W., Sun, L., Jiang, X., Hu, L., Xiong, S., Liu, T., Dong, X., Li, J., Jiang, Y., et al. (2020). Robust metal ion-chelated polymer interfacial layer for ultraflexible non-fullerene organic solar cells. Nat. Commun. *11*, 4508. 10.1038/s41467-020-18373-0.
10. Liu, B., Sun, H., Lee, J.-W., Jiang, Z., Qiao, J., Wang, J., Yang, J., Feng, K., Liao, Q., An, M., et al. (2023). Efficient and stable organic solar cells enabled by multicomponent photoactive layer based on one-pot polymerization. Nat. Commun. *14*, 967. 10.1038/s41467-023-36413-3.
11. Sun, C., Lee, J.W., Lee, C.Y., Lee, D.C., Cho, S.N., Kwon, S.K., Kim, B.J., and Kim, Y.H. (2023). Dimerized small-molecule acceptors enable efficient and stable organic solar cells. Joule *7*, 416-430. 10.1016/j.joule.2023.01.009.
12. Zeng, G., Chen, W., Chen, X., Hu, Y., Chen, Y., Zhang, B., Chen, H., Sun, W., Shen, Y., Li, Y., et al. (2022). Realizing 17.5% Efficiency Flexible Organic Solar Cells via Atomic-Level Chemical Welding of Silver Nanowire Electrodes. J. Am. Chem. Soc. *144*, 8658-8668. 10.1021/jacs.2c01503.
13. Song, W., Yu, K., Ge, J., Xie, L., Zhou, R., Peng, R., Zhang, X., Yang, M., Wei, Z., and Ge, Z. (2022). Entangled structure morphology by polymer guest enabling mechanically robust organic solar cells with efficiencies of over 16.5%. Matter *5*, 1877-1889. https://doi.org/10.1016/j.matt.2022.03.012.
14. Ma, L., Cui, Y., Zhang, J., Xian, K., Chen, Z., Zhou, K., Zhang, T., Wang, W., Yao, H., Zhang, S., et al. (2023). High-Efficiency and Mechanically Robust All-Polymer Organic Photovoltaic Cells Enabled by Optimized Fibril Network Morphology. Adv. Mater. *35*, 2208926. https://doi.org/10.1002/adma.202208926.
15. Song, W., Yu, K., Zhou, E., Xie, L., Hong, L., Ge, J., Zhang, J., Zhang, X., Peng, R., and Ge, Z. (2021). Crumple Durable Ultraflexible Organic Solar Cells with an Excellent Power-per-Weight Performance. Adv. Funct. Mater. *31*, 2102694. https://doi.org/10.1002/adfm.202102694.
16. Liang, Z., Li, M., Wang, Q., Qin, Y., Stuard, S.J., Peng, Z., Deng, Y., Ade, H., Ye, L., and Geng, Y. (2020). Optimization Requirements of Efficient Polythiophene:Nonfullerene Organic Solar Cells. Joule *4*, 1278-1295. https://doi.org/10.1016/j.joule.2020.04.014.
17. Azzouzi, M., Kirchartz, T., and Nelson, J. (2019). Factors Controlling Open-Circuit Voltage Losses in Organic Solar Cells. Trends Chem *1*, 49-62. 10.1016/j.trechm.2019.01.010.
18. Yuan, J., Zhang, H.T., Zhang, R., Wang, Y.M., Hou, J.H., Leclerc, M., Zhan, X.W., Huang, F., Gao, F., Zou, Y.P., and Li, Y.F. (2020). Reducing Voltage Losses in the A-DA'D-A Acceptor-Based Organic Solar Cells. Chem-Us *6*, 2147-2161. 10.1016/j.chempr.2020.08.003.
19. Fukuda, K., Yu, K., and Someya, T. (2020). The Future of Flexible Organic Solar Cells. Adv. Energy Mater. *10*, 2000765. https://doi.org/10.1002/aenm.202000765.

20. Chen, W., Zhu, Y., Xiu, J., Chen, G., Liang, H., Liu, S., Xue, H., Birgersson, E., Ho, J.W., Qin, X., et al. (2022). Monolithic perovskite/organic tandem solar cells with 23.6% efficiency enabled by reduced voltage losses and optimized interconnecting layer. Nat. Energy *7*, 229-237. 10.1038/s41560-021-00966-8.
21. Nguyen, T.-Q. (2022). Barrier to charge generation. Nat. Energy. 10.1038/s41560-022-01159-7.
22. Eisner, F.D., Azzouzi, M., Fei, Z., Hou, X., Anthopoulos, T.D., Dennis, T.J.S., Heeney, M., and Nelson, J. (2019). Hybridization of Local Exciton and Charge-Transfer States Reduces Nonradiative Voltage Losses in Organic Solar Cells. J. Am. Chem. Soc. *141*, 6362-6374. 10.1021/jacs.9b01465.
23. Lin, Y., Wang, J., Zhang, Z.G., Bai, H., Li, Y., Zhu, D., and Zhan, X. (2015). An electron acceptor challenging fullerenes for efficient polymer solar cells. Adv. Mater. *27*, 1170-1174.
24. Cheng, P., Li, G., Zhan, X., and Yang, Y.J.N.P. (2018). Next-generation organic photovoltaics based on non-fullerene acceptors. Nat. Photon. *12*, 131-142.
25. Lin, Y.Z., Zhao, F.W., He, Q., Huo, L.J., Wu, Y., Parker, T.C., Ma, W., Sun, Y.M., Wang, C.R., Zhu, D.B., et al. (2016). High-Performance Electron Acceptor with Thienyl Side Chains for Organic Photovoltaics. J. Am. Chem. Soc. *138*, 4955-4961. 10.1021/jacs.6b02004.
26. Yan, C., Barlow, S., Wang, Z., Yan, H., Jen, A.K.-Y., Marder, S.R., and Zhan, X. (2018). Non-fullerene acceptors for organic solar cells. Nat. Rev. Mater. *3*, 1-19.
27. Chandrabose, S., Chen, K., Barker, A.J., Sutton, J.J., Prasad, S.K.K., Zhu, J., Zhou, J., Gordon, K.C., Xie, Z., Zhan, X., and Hodgkiss, J.M. (2019). High Exciton Diffusion Coefficients in Fused Ring Electron Acceptor Films. J. Am. Chem. Soc. *141*, 6922-6929. 10.1021/jacs.8b12982.
28. Armin, A., Li, W., Sandberg, O.J., Xiao, Z., Ding, L., Nelson, J., Neher, D., Vandewal, K., Shoaee, S., Wang, T., et al. (2021). A History and Perspective of Non-Fullerene Electron Acceptors for Organic Solar Cells. Adv. Energy Mater. *11*, 2003570. https://doi.org/10.1002/aenm.202003570.
29. Yuan, J., Zhang, Y.Q., Zhou, L.Y., Zhang, G.C., Yip, H.L., Lau, T.K., Lu, X.H., Zhu, C., Peng, H.J., Johnson, P.A., et al. (2019). Single-Junction Organic Solar Cell with over 15% Efficiency Using Fused-Ring Acceptor with Electron-Deficient Core. Joule *3*, 1140-1151. 10.1016/j.joule.2019.01.004.
30. Yuan, J., Zhang, Y., Zhou, L., Zhang, C., Lau, T.K., Zhang, G., Lu, X., Yip, H.L., So, S.K., Beaupré, S., et al. (2019). Fused Benzothiadiazole: A Building Block for n-Type Organic Acceptor to Achieve High-Performance Organic Solar Cells. Adv. Mater. *31*, 1807577.
31. Li, G., Zhang, X., Jones, L.O., Alzola, J.M., Mukherjee, S., Feng, L.-W., Zhu, W., Stern, C.L., Huang, W., Yu, J., et al. (2021). Systematic Merging of Nonfullerene Acceptor π-Extension and Tetrafluorination Strategies Affords Polymer Solar Cells with >16% Efficiency. J. Am. Chem. Soc. *143*, 6123-6139. 10.1021/jacs.1c00211.
32. Li, C., Zhou, J., Song, J., Xu, J., Zhang, H., Zhang, X., Guo, J., Zhu, L., Wei, D., Han, G., et al. (2021). Non-fullerene acceptors with branched side chains and improved molecular packing to exceed 18% efficiency in organic solar cells. Nat. Energy *6*, 605-613. 10.1038/s41560-021-00820-x.
33. Li, G.P., Feng, L.W., Mukherjee, S., Jones, L.O., Jacobberger, R.M., Huang, W., Young,

R.M., Pankow, R.M., Zhu, W.G., Lu, N., et al. (2022). Non-fullerene acceptors with direct and indirect hexa-fluorination afford > 17% efficiency in polymer solar cells. Energy Environ. Sci. *15*, 645-659. 10.1039/d1ee03225a.

34. Luo, Z., Gao, Y., Lai, H., Li, Y., Wu, Z., Chen, Z., Sun, R., Ren, J., Zhang, C.e., He, F., et al. (2022). Asymmetric side-chain substitution enables a 3D network acceptor with hydrogen bond assisted crystal packing and enhanced electronic coupling for efficient organic solar cells. Energy Environ. Sci. *15*, 4601-4611. 10.1039/D2EE01848A.
35. Chen, H., Zhao, T., Li, L., Tan, P., Lai, H., Zhu, Y., Lai, X., Han, L., Zheng, N., Guo, L., and He, F. (2021). 17.6%-Efficient Quasiplanar Heterojunction Organic Solar Cells from a Chlorinated 3D Network Acceptor. Adv. Mater. *33*, 2102778. https://doi.org/10.1002/adma.202102778.
36. Cheng, P., Liu, Y., Chang, S.-Y., Li, T., Sun, P., Wang, R., Cheng, H.-W., Huang, T., Meng, L., Nuryyeva, S., et al. (2019). Efficient Tandem Organic Photovoltaics with Tunable Rear Sub-cells. Joule *3*, 432-442. 10.1016/j.joule.2018.11.011.
37. Gao, W., Qi, F., Peng, Z., Lin, F.R., Jiang, K., Zhong, C., Kaminsky, W., Guan, Z., Lee, C.-S., Marks, T.J., et al. (2022). Achieving 19% Power Conversion Efficiency in Planar-Mixed Heterojunction Organic Solar Cells Using a Pseudosymmetric Electron Acceptor. Adv. Mater. *34*, 2202089. https://doi.org/10.1002/adma.202202089.
38. Li, Y., Cai, Y.H., Xie, Y.P., Song, J.H., Wu, H.B., Tang, Z., Zhang, J., Huang, F., and Sun, Y.M. (2021). A facile strategy for third-component selection in non-fullerene acceptor-based ternary organic solar cells. Energy Environ. Sci. *14*, 5009-5016. 10.1039/d1ee01864g.
39. Zhu, L., Zhang, M., Xu, J., Li, C., Yan, J., Zhou, G., Zhong, W., Hao, T., Song, J., Xue, X., et al. (2022). Single-junction organic solar cells with over 19% efficiency enabled by a refined double-fibril network morphology. Nat. Mater. *21*, 656-663. 10.1038/s41563-022-01244-y.
40. Liao, C.-Y., Chen, Y., Lee, C.-C., Wang, G., Teng, N.-W., Lee, C.-H., Li, W.-L., Chen, Y.-K., Li, C.-H., and Ho, H.-L. (2020). Processing strategies for an organic photovoltaic module with over 10% efficiency. Joule *4*, 189-206.
41. Li, B., Zhang, X., Wu, Z., Yang, J., Liu, B., Liao, Q., Wang, J., Feng, K., Chen, R., Woo, H.Y., et al. (2022). Over 16% efficiency all-polymer solar cells by sequential deposition. Sci. China Chem. *65*, 1157-1163. 10.1007/s11426-022-1247-1.
42. Lopez, S.A., Sanchez-Lengeling, B., Soares, J.D., and Aspuru-Guzik, A. (2017). Design Principles and Top Non-Fullerene Acceptor Candidates for Organic Photovoltaics. Joule *1*, 857-870. 10.1016/j.joule.2017.10.006.
43. Zhang, X.H., Li, G.P., Mukherjee, S., Huang, W., Zheng, D., Feng, L.W., Chen, Y., Wu, J.L., Sangwan, V.K., Hersam, M.C., et al. (2022). Systematically Controlling Acceptor Fluorination Optimizes Hierarchical Morphology, Vertical Phase Separation, and Efficiency in Non-Fullerene Organic Solar Cells. Adv. Energy Mater. *12*. ARTN 2102172 10.1002/aenm.202102172.
44. Wu, J., Chen, Y., Liu, J., Pang, Z., Li, G., Lu, Z., Huang, Y., Facchetti, A., and Marks, T.J. (2022). Tuning the antiaromatic character and charge transport of pentalene-based antiaromatic compounds by substitution. J. Mater. Chem. C . *10*, 2724-2731. 10.1039/D1TC03156B.
45. Gao, W., Zhang, M., Liu, T., Ming, R.J., An, Q.S., Wu, K.L., Xie, D.J., Luo, Z.H., Zhong, C.,

Liu, F., et al. (2018). Asymmetrical Ladder-Type Donor-Induced Polar Small Molecule Acceptor to Promote Fill Factors Approaching 77% for High-Performance Nonfullerene Polymer Solar Cells. Adv. Mater. *30*. ARTN 1800052 10.1002/adma.201800052.

46. Li, S.X., Zhan, L.L., Sun, C.K., Zhu, H.M., Zhou, G.Q., Yang, W.T., Shi, M.M., Li, C.Z., Hou, J.H., Li, Y.F., and Chen, H.Z. (2019). Highly Efficient Fullerene-Free Organic Solar Cells Operate at Near Zero Highest Occupied Molecular Orbital Offsets. J. Am. Chem. Soc. *141*, 3073-3082. 10.1021/jacs.8b12126.
47. Li, S., Zhan, L., Jin, Y., Zhou, G., Lau, T.-K., Qin, R., Shi, M., Li, C.-Z., Zhu, H., Lu, X., et al. (2020). Asymmetric Electron Acceptors for High-Efficiency and Low-Energy-Loss Organic Photovoltaics. Adv. Mater. *32*, 2001160. 10.1002/adma.202001160.
48. Luo, Z.H., Ma, R.J., Liu, T., Yu, J.W., Xiao, Y.Q., Sun, R., Xie, G.S., Yuan, J., Chen, Y.Z., Chen, K., et al. (2020). Fine-Tuning Energy Levels via Asymmetric End Groups Enables Polymer Solar Cells with Efficiencies over 17%. Joule *4*, 1236-1247. 10.1016/j.joule.2020.03.023.
49. Li, D.X., Sun, C.Y., Yan, T.F., Yuan, J., and Zou, Y.P. (2021). Asymmetric Non-Fullerene Small-Molecule Acceptors toward High-Performance Organic Solar Cells. Acs Central Sci *7*, 1787-1797.
50. He, C., Chen, Z., Wang, T., Shen, Z., Li, Y., Zhou, J., Yu, J., Fang, H., Li, Y., Li, S., et al. (2022). Asymmetric electron acceptor enables highly luminescent organic solar cells with certified efficiency over 18%. Nat. Commun. *13*, 2598. 10.1038/s41467-022-30225-7.
51. Dai, S.X., Zhao, F.W., Zhang, Q.Q., Lau, T.K., Li, T.F., Liu, K., Ling, Q.D., Wang, C.R., Lu, X.H., You, W., and Zhan, X.W. (2017). Fused Nonacyclic Electron Acceptors for Efficient Polymer Solar Cells. J. Am. Chem. Soc. *139*, 1336-1343. 10.1021/jacs.6b12755.
52. Swick, S.M., Zhu, W.G., Matta, M., Aldrich, T.J., Harbuzaru, A., Navarrete, J.T.L., Ortiz, R.P., Kohlstedt, K.L., Schatz, G.C., Facchetti, A., et al. (2018). Closely packed, low reorganization energy pi-extended postfullerene acceptors for efficient polymer solar cells. Proc. Natl. Acad. Sci. U.S.A. *115*, E8341-E8348. 10.1073/pnas.1807535115.
53. Aldrich, T.J., Matta, M., Zhu, W.G., Swick, S.M., Stern, C.L., Schatz, G.C., Facchetti, A., Melkonyan, F.S., and Marks, T.J. (2019). Fluorination Effects on Indacenodithienothiophene Acceptor Packing and Electronic Structure, End-Group Redistribution, and Solar Cell Photovoltaic Response. J. Am. Chem. Soc. *141*, 3274-3287. 10.1021/jacs.8b13653.
54. Liu, X., Rand, B.P., and Forrest, S.R. (2019). Engineering Charge-Transfer States for Efficient, Low-Energy-Loss Organic Photovoltaics. Trends Chem *1*, 815-829. 10.1016/j.trechm.2019.08.001.
55. Jones, M.L., Dyer, R., Clarke, N., and Groves, C. (2014). Are hot charge transfer states the primary cause of efficient free-charge generation in polymer: fullerene organic photovoltaic devices? A kinetic Monte Carlo study. Phys. Chem. Chem. Phys. *16*, 20310-20320. 10.1039/c4cp01626b.
56. Zhu, W., Alzola, J.M., Aldrich, T.J., Kohlstedt, K.L., Zheng, D., Hartnett, P.E., Eastham, N.D., Huang, W., Wang, G., Young, R.M., et al. (2019). Fluorine Tuning of Morphology, Energy Loss, and Carrier Dynamics in Perylenediimide Polymer Solar Cells. ACS Energy Lett. *4*, 2695-2702. 10.1021/acsenergylett.9b02146.
57. Azzouzi, M., Gallop, N.P., Eisner, F., Yan, J., Zheng, X., Cha, H., He, Q., Fei, Z., Heeney, M.,

Bakulin, A.A., and Nelson, J. (2022). Reconciling models of interfacial state kinetics and device performance in organic solar cells: impact of the energy offsets on the power conversion efficiency. Energy Environ. Sci. *15*, 1256-1270. 10.1039/D1EE02788C.

58. Lai, H., Lai, X., Chen, Z.-Y., Zhu, Y., Wang, H., Chen, H., Tan, P., Zhu, Y., Zhang, Y., and He, F. (2022). Crystallography, Packing Mode, and Aggregation State of Chlorinated Isomers for Efficient Organic Solar Cells. CCS Chem. *5*, 1118-1129. 10.31635/ccschem.022.202201875.
59. Gao, W., Qi, F., Peng, Z., Lin, F.R., Jiang, K., Zhong, C., Kaminsky, W., Guan, Z., Lee, C.-S., Marks, T.J., et al. (2022). Achieving 19% Power Conversion Efficiency in Planar-Mixed Heterojunction Organic Solar Cells Using a Pseudosymmetric Electron Acceptor. Adv. Mater. *34*, 2202089. https://doi.org/10.1002/adma.202202089.
60. Xu, J., Lin, F., Zhu, L., Zhang, M., Hao, T., Zhou, G., Gao, K., Zou, Y., Wei, G., Yi, Y., et al. (2022). The Crystalline Behavior and Device Function of Nonfullerene Acceptors in Organic Solar Cells. Adv. Energy Mater. *12*, 2201338. https://doi.org/10.1002/aenm.202201338.
61. Lai, H.J., Zhao, Q.Q., Chen, Z.Y., Chen, H., Chao, P.J., Zhu, Y.L., Lang, Y.W., Zhen, N., Mo, D.Z., Zhang, Y.Z., and He, F. (2020). Trifluoromethylation Enables a 3D Interpenetrated Low-Band-Gap Acceptor for Efficient Organic Solar Cells. Joule *4*, 688-700. 10.1016/j.joule.2020.02.004.
62. Holliday, S., Ashraf, R.S., Nielsen, C.B., Kirkus, M., Rohr, J.A., Tan, C.H., Collado-Fregoso, E., Knall, A.C., Durrant, J.R., Nelson, J., and McCulloch, I. (2015). A Rhodanine Flanked Nonfullerene Acceptor for Solution-Processed Organic Photovoltaics. J. Am. Chem. Soc. *137*, 898-904.
63. Ahn, J., Oh, S., Lee, H., Lee, S., Song, C.E., Lee, H.K., Lee, S.K., So, W.-W., Moon, S.-J., Lim, E., et al. (2019). Simple and Versatile Non-Fullerene Acceptor Based on Benzothiadiazole and Rhodanine for Organic Solar Cells. ACS Appl. Mater. Interfaces. *11*, 30098-30107. 10.1021/acsami.9b09256.
64. Kim, Y., Song, C.E., Ko, E.J., Kim, D., Moon, S.J., and Lim, E. (2015). DPP-based small molecule, non-fullerene acceptors for “channel II” charge generation in OPVs and their improved performance in ternary cells. Rsc Adv *5*, 4811-4821. 10.1039/C4RA12184H.
65. Mamone, M., Bura, T., Brassard, S., Soligo, E., He, K.Q., Li, Y.N., and Leclerc, M. (2020). Optimized synthesis of fluorinated dithienyl-diketopyrrolopyrroles and new copolymers obtained via direct heteroarylation polymerization. Mater. Chem. Front. *4*, 2040-2046. 10.1039/d0qm00218f.
66. Zhao, C., Guo, Y., Zhang, Y., Yan, N., You, S., and Li, W. (2019). Diketopyrrolopyrrole-based conjugated materials for non-fullerene organic solar cells. J. Mater. Chem. A . *7*, 10174-10199. 10.1039/C9TA01976F.
67. Rao, P.S., Gupta, A., Srivani, D., Bhosale, S.V., Bilic, A., Li, J., Xiang, W., Evans, R.A., and Bhosale, S.V. (2018). An efficient non-fullerene acceptor based on central and peripheral naphthalene diimides. Chem. Commun. *54*, 5062-5065. 10.1039/C8CC01779D.
68. Zhou, N., Dudnik, A.S., Li, T.I.N.G., Manley, E.F., Aldrich, T.J., Guo, P., Liao, H.-C., Chen, Z., Chen, L.X., Chang, R.P.H., et al. (2016). All-Polymer Solar Cell Performance Optimized via Systematic Molecular Weight Tuning of Both Donor and Acceptor Polymers. J. Am. Chem. Soc. *138*, 1240-1251. 10.1021/jacs.5b10735.

69. Zhang, X., Li, G., Mukherjee, S., Huang, W., Zheng, D., Feng, L.-W., Chen, Y., Wu, J., Sangwan, V.K., Hersam, M.C., et al. (2022). Systematically Controlling Acceptor Fluorination Optimizes Hierarchical Morphology, Vertical Phase Separation, and Efficiency in Non-Fullerene Organic Solar Cells. Adv. Energy Mater. *12*, 2102172. https://doi.org/10.1002/aenm.202102172.

70. Holliday, S., Ashraf, R.S., Wadsworth, A., Baran, D., Yousaf, S.A., Nielsen, C.B., Tan, C.H., Dimitrov, S.D., Shang, Z.R., Gasparini, N., et al. (2016). High-efficiency and air-stable P3HT-based polymer solar cells with a new non-fullerene acceptor. Nat. Commun. *7*. ARTN 11585
10.1038/ncomms11585.

71. Zhang, C.H., Heumueller, T., Gruber, W., Almora, O., Du, X.Y., Ying, L., Chen, J.W., Unruh, T., Cao, Y., Li, N., and Brabec, C.J. (2019). Comprehensive Investigation and Analysis of Bulk-Heterojunction Microstructure of High-Performance PCE11:PCBM Solar Cells. ACS Appl. Mater. Interfaces. *11*, 18555-18563. 10.1021/acsami.8b22539.

72. Cheng, P., Hou, J.H., Li, Y.F., and Zhan, X.W. (2014). Layer-by-Layer Solution-Processed Low-Bandgap Polymer-PC61BM Solar Cells with High Efficiency. Adv. Energy Mater. *4*. ARTN 1301349
10.1002/aenm.201301349.

73. Miller, O.D., Yablonovitch, E., and Kurtz, S.R. (2012). Strong Internal and External Luminescence as Solar Cells Approach the Shockley-Queisser Limit. Ieee J Photovolt *2*, 303-311. 10.1109/Jphotov.2012.2198434.

74. Chen, J., Liao, Q., Wang, G., Yan, Z., Wang, H., Wang, Y., Zhang, X., Tang, Y., Facchetti, A., Marks, T.J., and Guo, X. (2018). Enhancing Polymer Photovoltaic Performance via Optimized Intramolecular Ester-Based Noncovalent Sulfur···Oxygen Interactions. Macromolecules *51*, 3874-3885. 10.1021/acs.macromol.8b00161.

75. Swick, S.M., Alzola, J.M., Sangwan, V.K., Amsterdam, S.H., Zhu, W., Jones, L.O., Powers-Riggs, N., Facchetti, A., Kohlstedt, K.L., Schatz, G.C., et al. (2020). Fluorinating π-Extended Molecular Acceptors Yields Highly Connected Crystal Structures and Low Reorganization Energies for Efficient Solar Cells. Adv. Energy Mater. *10*, 2000635. 10.1002/aenm.202000635.

76. Rivnay, J., Noriega, R., Kline, R.J., Salleo, A., and Toney, M.F. (2011). Quantitative analysis of lattice disorder and crystallite size in organic semiconductor thin films. Phys. Rev. B . *84*. ARTN 045203
10.1103/PhysRevB.84.045203.

77. Zhu, W.G., Spencer, A.P., Mukherjee, S., Alzola, J.M., Sangwan, V.K., Amsterdam, S.H., Swick, S.M., Jones, L.O., Heiber, M.C., Herzing, A.A., et al. (2020). Crystallography, Morphology, Electronic Structure, and Transport in Non-Fullerene/Non-Indacenodithienothiophene Polymer:Y6 Solar Cells. J. Am. Chem. Soc. *142*, 14532-14547. 10.1021/jacs.0c05560.

78. Eastham, N.D., Logsdon, J.L., Manley, E.F., Aldrich, T.J., Leonardi, M.J., Wang, G., Powers-Riggs, N.E., Young, R.M., Chen, L.X., Wasielewski, M.R., et al. (2018). Hole-Transfer Dependence on Blend Morphology and Energy Level Alignment in Polymer: ITIC Photovoltaic Materials. Adv. Mater. *30*. UNSP 1704263
10.1002/adma.201704263.

79. Zheng, Z., Awartani, O.M., Gautam, B., Liu, D., Qin, Y., Li, W., Bataller, A., Gundogdu, K., Ade, H., and Hou, J. (2017). Efficient Charge Transfer and Fine-Tuned Energy Level Alignment in a THF-Processed Fullerene-Free Organic Solar Cell with 11.3% Efficiency. Adv. Mater. *29*, 1604241. https://doi.org/10.1002/adma.201604241.
80. Zhu, L., Zhang, M., Zhou, G., Hao, T., Xu, J., Wang, J., Qiu, C., Prine, N., Ali, J., Feng, W., et al. (2020). Efficient Organic Solar Cell with 16.88% Efficiency Enabled by Refined Acceptor Crystallization and Morphology with Improved Charge Transfer and Transport Properties. Adv. Energy Mater. *10*, 1904234. https://doi.org/10.1002/aenm.201904234.
81. Liu, J., Chen, S., Qian, D., Gautam, B., Yang, G., Zhao, J., Bergqvist, J., Zhang, F., Ma, W., Ade, H., et al. (2016). Fast charge separation in a non-fullerene organic solar cell with a small driving force. Nat. Energy *1*, 16089. 10.1038/nenergy.2016.89.
82. Cheng, P., Zhang, M., Lau, T.-K., Wu, Y., Jia, B., Wang, J., Yan, C., Qin, M., Lu, X., and Zhan, X. (2017). Realizing Small Energy Loss of 0.55 eV, High Open-Circuit Voltage >1 V and High Efficiency >10% in Fullerene-Free Polymer Solar Cells via Energy Driver. Adv. Mater. *29*, 1605216. https://doi.org/10.1002/adma.201605216.
83. Hu, Q., Chen, W., Yang, W., Li, Y., Zhou, Y., Larson, B.W., Johnson, J.C., Lu, Y.-H., Zhong, W., Xu, J., et al. (2020). Improving Efficiency and Stability of Perovskite Solar Cells Enabled by A Near-Infrared-Absorbing Moisture Barrier. Joule *4*, 1575-1593. https://doi.org/10.1016/j.joule.2020.06.007.
84. Liang, S., Li, S., Zhang, Y., Li, T., Zhou, H., Jin, F., Sheng, C., Ni, G., Yuan, J., Ma, W., and Zhao, H. (2021). Efficient Hole Transfer via Delocalized Excited State in Small Molecular Acceptor: A Comparative Study on Photodynamics of PM6:Y6 and PM6:ITIC Organic Photovoltaic Blends. Adv. Funct. Mater. *31*, 2102764. https://doi.org/10.1002/adfm.202102764.
85. Zuo, L., Jo, S.B., Li, Y., Meng, Y., Stoddard, R.J., Liu, Y., Lin, F., Shi, X., Liu, F., Hillhouse, H.W., et al. (2022). Dilution effect for highly efficient multiple-component organic solar cells. Nat. Nanotechnol. *17*, 53-60. 10.1038/s41565-021-01011-1.
86. Gillett, A.J., Privitera, A., Dilmurat, R., Karki, A., Qian, D., Pershin, A., Londi, G., Myers, W.K., Lee, J., Yuan, J., et al. (2021). The role of charge recombination to triplet excitons in organic solar cells. Nature *597*, 666-671. 10.1038/s41586-021-03840-5.
87. Zhang, W.C., Huang, J.H., Xu, J.Q., Han, M.M., Su, D., Wu, N.N., Zhang, C.F., Xu, A.J., and Zhan, C.L. (2020). Phthalimide Polymer Donor Guests Enable over 17% Efficient Organic Solar Cells via Parallel-Like Ternary and Quaternary Strategies. Adv. Energy Mater. *10*. ARTN 2001436
10.1002/aenm.202001436.
88. Liu, T., Huo, L.J., Chandrabose, S., Chen, K., Han, G.C., Qi, F., Meng, X.Y., Xie, D.J., Ma, W., Yi, Y.P., et al. (2018). Optimized Fibril Network Morphology by Precise Side-Chain Engineering to Achieve High-Performance Bulk-Heterojunction Organic Solar Cells. Adv. Mater. *30*. ARTN 1707353
10.1002/adma.201707353.
89. Wang, R., Yao, Y., Zhang, C.F., Zhang, Y.D., Bin, H.J., Xue, L.W., Zhang, Z.G., Xie, X.Y., Ma, H.B., Wang, X.Y., et al. (2019). Ultrafast hole transfer mediated by polaron pairs in all-polymer photovoltaic blends. Nat. Commun. *10*. ARTN 398
10.1038/s41467-019-08361-4.

90. Su, N., Ma, R., Li, G., Liu, T., Feng, L.-W., Lin, C., Chen, J., Song, J., Xiao, Y., Qu, J., et al. (2021). High-Efficiency All-Polymer Solar Cells with Poly-Small-Molecule Acceptors Having π-Extended Units with Broad Near-IR Absorption. ACS Energy Lett. *6*, 728-738.
91. Heiber, M.C., Okubo, T., Ko, S.J., Luginbuhl, B.R., Ran, N.A., Wang, M., Wang, H.B., Uddin, M.A., Woo, H.Y., Bazan, G.C., and Nguyen, T.Q. (2018). Measuring the competition between bimolecular charge recombination and charge transport in organic solar cells under operating conditions. Energy Environ. Sci. *11*, 3019-3032. 10.1039/c8ee01559g.
92. Bartesaghi, D., Perez, I.D., Kniepert, J., Roland, S., Turbiez, M., Neher, D., and Koster, L.J.A. (2015). Competition between recombination and extraction of free charges determines the fill factor of organic solar cells. Nat. Commun. *6*, 7083. ARTN 7083 10.1038/ncomms8083.
93. Feng, L.W., Chen, J.H., Mukherjee, S., Sangwan, V.K., Huang, W., Chen, Y., Zheng, D., Strzalka, J.W., Wang, G., Hersam, M.C., et al. (2020). Readily Accessible Benzo[d]thiazole Polymers for Nonfullerene Solar Cells with > 16% Efficiency and Potential Pitfalls. ACS Energy Lett. *5*, 1780-1787. 10.1021/acsenergylett.0c00691.

Graphical Abstract